
# A novel double Z-scheme photocatalyst $Ag_3PO_4/Bi_2S_3/Bi_2O_3$ with enhanced visible-light photocatalytic performance for antibiotic degradation

Binbin Shao, Xiaojuan Liu, Zhifeng Liu, Guangming Zeng, Qinghua Liang, Chao Liang, Ying Cheng, Wei Zhang, Yang Liu, Shanxi Gong

PII: S1385-8947(19)30478-4
DOI: https://doi.org/10.1016/j.cej.2019.03.013
Reference: CEJ 21137

To appear in: *Chemical Engineering Journal*

Received Date: 16 November 2018
Revised Date: 10 February 2019
Accepted Date: 2 March 2019

Please cite this article as: B. Shao, X. Liu, Z. Liu, G. Zeng, Q. Liang, C. Liang, Y. Cheng, W. Zhang, Y. Liu, S. Gong, A novel double Z-scheme photocatalyst $Ag_3PO_4/Bi_2S_3/Bi_2O_3$ with enhanced visible-light photocatalytic performance for antibiotic degradation, *Chemical Engineering Journal* (2019), doi: https://doi.org/10.1016/j.cej.2019.03.013

# A novel double Z-scheme photocatalyst $Ag_3PO_4/Bi_2S_3/Bi_2O_3$ with enhanced visible-light photocatalytic performance for antibiotic degradation

Binbin Shao [a,1], Xiaojuan Liu [b,1], Zhifeng Liu [a,1,*], Guangming Zeng [a,*], Qinghua Liang [a], Chao Liang [a], Ying Cheng [a], Wei Zhang [b], Yang Liu [a], Shanxi Gong [c]

[a] College of Environmental Science and Engineering, Hunan University and Key Laboratory of Environmental Biology and Pollution Control (Hunan University), Ministry of Education, Changsha 410082, P.R. China

[b] The First Affiliated Hospital of Hunan University of Chinese Medicine, Changsha 410007, P.R. China.

[c] School of Chemistry and Chemical Engineering of Guangxi University, Nanning 530004, PR China.

* Corresponding authors at:

[a] College of Environmental Science and Engineering, Hunan University and Key Laboratory of Environmental Biology and Pollution Control (Hunan University), Ministry of Education, Changsha 410082, P.R. China

E-mail: zhifengliu@hnu.edu.cn (Z. Liu)

E-mail: zgming@hnu.edu.cn (G. Zeng)

[1] The authors contribute equally to this paper.

**Abstract**

In this study, the novel visible light double Z-scheme photocatalysts ($Ag_3PO_4/Bi_2S_3/Bi_2O_3$) were synthesized by the facile means. The crystal texture, chemical states, morphology and optical characteristics of prepared photocatalysts were investigated by XRD, FTIR, XPS, SEM, TEM, $N_2$ adsorption-desorption analysis, UV-vis DRS, and PL etc. techniques, respectively. Meanwhile, the band structures and the density of states of three single-phase semiconductor and $Ag_3PO_4/Bi_2S_3/Bi_2O_3$ (ABB) composite had been calculated by Materials Studio program based on density functional theory. For assessing the photocatalytic performance of these samples, the visible light photodegradation of antibiotics sulfamethazine (SAZ) and cloxacillin (CLX) were performed. The effects of initial antibiotic concentration, reaction pH, supporting electrolyte and surfactant on photocatalytic performance were all investigated. The results indicated that the ABB-3 composite exhibited higher photocatalytic performance than other comparison samples. Furthermore, four cycle experiments confirmed the ABB-3 composite also exhibited satisfactory photostability. The scavenger tests and ESR data demonstated that the active species $h^+$, $\cdot O_2^-$, and ·OH worked together in the photocatalytic process, and the $h^+$ and $\cdot O_2^-$ play a more important role than ·OH. All in all, the increased photocatalytic performance of ABB composite could owe to the photosensitization of $Bi_2S_3$ and the double Z-scheme photocatalytic system. This study could inspire some new idea for building the novel and efficient heterogeneous photocatalysts and

benefiting their practical application.

**Keywords:** $Ag_3PO_4/Bi_2S_3/Bi_2O_3$; Density functional theory; Photosensitization; Double Z-scheme photocatalytic system; Visible light; Antibiotics.

## 1. Introduction

Over the past decades, the antibiotics have been frequently detected in natural water, sewage effluent, soils and sediments because of their overusing [1]. According to some previous studies the concentration of antibiotics in the environment is ng $L^{-1}$ level to μg $L^{-1}$ level generally [2]. However, in some times, the concentration of antibiotics can reach mg $L^{-1}$ level in effluents [3]. These emerging micropollutants can cause harm to environmental and human due to their possible role in the development of antibiotic-resistant bacteria [1]. Therefore, it is necessary to employ an effective method to eliminate antibiotic pollution. Compared to some traditional methods, recently, the semiconductor photocatalysis technique has gained great interest in the photodegradation of organic pollutants due to their low cost, efficient, and environmental friendly [1, 4, 5]. To date, numerous semiconductor materials have shown the potential for the practical applications, and they could be divided into two categories based on the ingredients, namely metal-based photocatalysts (such as $TiO_2$ [6], ZnO [7], $WO_3$ [8], $BiVO_4$ [9], $Ag_3PO_4$ [10], $Bi_2S_3$ [11], CdS [12], etc.) and metal-free photocatalysts (such as carbon nitride [13], polyaniline [14], phosphorus [15] etc.).

Among these photocatalysts, recently, a great deal of attention has been paid to

the silver-based semiconductors. The $Ag_3PO_4$, an important silver-based photocatalyst, it possesses a narrow band gap ($E_g$, about 2.40 eV) and high visible light response. Many studies indicated that the $Ag_3PO_4$ exhibits high photocatalytic performance in pollutant removal and $O_2$ evolution from water under visible light illumination. The quantum efficiency could be up to 90% of $O_2$ evolution reaction at wavelengths more than 420 nm for $Ag_3PO_4$ [8, 10, 16]. However, it is still a big challenge for the practical application of a single $Ag_3PO_4$ photocatalyst, which is mainly because of the uncontrollable photocorrosion by the photogenerated electron-hole ($e^-$-$h^+$) pairs ($4Ag_3PO_4 + 6H_2O + 12h^+ + 12e^- \rightarrow 12Ag + 4H_3PO_4 + 3O_2$) and the speedy recombination of photogenerated $e^-$-$h^+$ pairs [6, 9, 17]. For overcoming those constraints, various strategies have been proposed and used, a promising strategy is combined $Ag_3PO_4$ with others semiconductors to construct a heterojunction photocatalytic system [8, 18, 19]. For example, Liu et al. [8] had prepared the $Ag_3PO_4/WO_3$ heterojunction photocatalyst by the deposition-precipitation method, and this photocatalyst showed high photocatalytic performance for rhodamine B (RhB) degradation. Fu et al. [20] had prepared the $Ag_3PO_4/Bi_2WO_6$ heterojunction for the efficient photocatalytic of phenol under visible light illumination. Compared to the single semiconductors, the increased photocatalytic performance of these composites could owe to the high photostability and fast separation of photogenerated $e^-$-$h^+$ pairs.

The $Bi_2O_3$, a favorable bismuth-based semiconductor photocatalyst because of the credible stability, excellent optical characteristics, low/non-toxicity and easy availability [1, 21]. Recently, the $Bi_2O_3$ has been intensively studied due to the narrow

$E_g$ (about 2.80 eV) and perform high visible light photocatalytic performance due to the hybridized O 2p and Bi $6s^2$ valence bands [22, 23]. Especially, the valence band (VB) edge of $Bi_2O_3$ (3.13 V vs NHE) is enough positive potential to oxidize $OH^-$ or $H_2O$ to form ·OH ($OH^-$/·OH (2.40 eV) and $H_2O$/·OH (2.72 eV)) [24]. The $Bi_2S_3$, another important bismuth-based semiconductor, it possesses a very narrow $E_g$ of about 1.3 eV. More strikingly, the $Bi_2S_3$ exhibits photosensitization in the visible light region, which contributes to improving the visible light response of others materials after forming heterojunction [11, 21, 25, 26]. Furthermore, some studies reported that the photocorrosion of some semiconductors (such as CdS, $Ag_2CO_3$, $Ag_3PO_4$) could be distinctively suppressed by combining the $Bi_2S_3$ [12, 27, 28].

Up to date, there are many studies on the binary heterojunction of $Ag_3PO_4$ and bismuth-based semiconductors, such as $Ag_3PO_4/Bi_2WO_6$ [18, 20], $Ag_3PO_4$/BiOX (X=Br, I, Cl) [29-31], $Ag_3PO_4/BiXO_4$ (X=P, V) [9, 32]. Compared to the single semiconductor system, the binary heterojunction system exhibited superior photocatalytic performance because of the higher efficiency of transfer and separation of the photoexcited $e^-$-$h^+$ pairs. Similar to the binary heterojunction, the ternary heterojunction could also possess excellent photocatalytic performance [6, 9]. Zhang et al. [33] reported that the $SrTiO_3/Ag/Ag_3PO_4$ ternary heterojunction performed excellent photocatalytic performance for degrading organic pollutants (RhB, MB and phenol) under visible light illumination due to the notably promoted separate efficiency of photoexcited $e^-$-$h^+$ pairs. Zhou et al. [34] reported that the ternary visible light driven photocatalyst $AgCl/Ag_3PO_4/g\text{-}C_3N_4$ performed the outstanding

photocatalytic performance in the degradation of sulfamethoxazole due to the rapid transfer and separation of photoexcited $e^-$-$h^+$ pairs and there is almost no photocorrosion occurs of $Ag_3PO_4$. However, so far, it is lack of research on ternary heterojunction of $Ag_3PO_4$ and bismuth-based semiconductors.

On account of the optical properties and good band potential matching between $Ag_3PO_4$, $Bi_2S_3$ and $Bi_2O_3$, in this study, the ternary visible light driven photocatalyst $Ag_3PO_4/Bi_2S_3/Bi_2O_3$ composite was prepared. The crystal, morphology, and optical characteristics of the as-prepared samples were investigated by XRD, FTIR, XPS, SEM, TEM, $N_2$ adsorption-desorption analysis, UV-vis DRS, PL, etc. techniques. Meanwhile, the theoretical calculations based on density functional theory were introduced to using Cambridge Serial Total Energy Package (CASTEP) method of Materials Studio (MS) program (DFT). Subsequently, the photocatalytic performance of the obtained samples was assessed towards antibiotics degradation under visible light illumination. Furthermore, the photoexcited charge migration and separation of $Ag_3PO_4/Bi_2S_3/Bi_2O_3$ composite and the degradation mechanism of antibiotics were discussed. It is hoped that this photocatalyst can be an ideal candidate for eliminating environmental pollutants and environmental remediation.

## 2. Experimental

### 2.1. Materials

Bismuth nitrate pentahydrate ($Bi(NO_3)_3 \cdot 5H_2O$), thiourea, silver nitrate ($AgNO_3$), disodium hydrogen phosphate dodecahydrate ($Na_2HPO_4 \cdot 12H_2O$), sulfamethazine

(SAZ) and cloxacillin (CLX) were obtained from J&K Scientific (Massachusetts, USA). Triethanolamine (TEA), p-benzoquinone (BQ), and isopropanol (IPA) were purchased from Ainopharm Chemical Reagent Co., Ltd. All other reagents were analytical grade and used on further purification. The deionized water (18.25 MΩ $cm^{-1}$) was used in the whole experiment.

### 2.2. Synthesis of $Bi_2O_3$, $Bi_2S_3/Bi_2O_3$ and $Ag_3PO_4/Bi_2S_3/Bi_2O_3$

The $Bi_2O_3$ (BO) was prepared as follows: 5.00 g of $Bi(NO_3)_3 \cdot 5H_2O$ was placed in a crucible, then they were calcined at 550 °C (2.3 °C $min^{-1}$) under $N_2$ atmosphere for 4 h in a tube furnace [1]. For fabricating the $Bi_2S_3/Bi_2O_3$ (BB) composite, typically, 1.864 g of BO was dispersed in 50 mL of ultrapure water, which including 0.228 g of thiourea. Then, the mixture was moved into an autoclave and maintained at 160 ºC for 6 h. Finally, the black composite was obtained [11]. For comparison, the pure $Bi_2S_3$ (BS) was also prepared and the process is similar to that of BB composite except that a higher amount of thiourea (2.736 g) was used.

The $Ag_3PO_4/Bi_2S_3/Bi_2O_3$ (ABB) was prepared as follows: 0.5 g of BB was dispersed in 50 mL of ultrapure water, and then, a certain amount of (0.030 g, 0.061 g, 0.122 g, 0.183 g) of $AgNO_3$ was added to the mixture quickly and violently stirred for 30 min under dark condition. Subsequently, 20 mL of $Na_2HPO_4$ solution (0.15 M) was injected into the mixture dropwise. Finally, the mixture was stirring for 1 h under dark condition, then the different content $Ag_3PO_4$ of ABB composites (5%-$Ag_3PO_4/Bi_2S_3/Bi_2O_3$, 10%-$Ag_3PO_4/Bi_2S_3/Bi_2O_3$, 20%-$Ag_3PO_4/Bi_2S_3/Bi_2O_3$,

30%-$Ag_3PO_4/Bi_2S_3/Bi_2O_3$) were obtained, and they were labeled as ABB-1, ABB-2, ABB-3, ABB-4, respectively [9]. For comparison, the pure $Ag_3PO_4$ (AP) and $Ag_3PO_4/Bi_2O_3$ (AB) composite were prepared with the same steps. In detail, the AP only used $AgNO_3$ as the precursor, and the AB used BO and $AgNO_3$ as the precursors. The schematic illustration of the preparation process of the $Ag_3PO_4/Bi_2S_3/Bi_2O_3$ composite was displayed in Fig. 1.

### 2.3. Characterization

The samples morphology and structure were investigated through field emission scanning electron microscope (FESEM, FEI, Quanta-F250) and transmission electron microscope (TEM, FEI, Tecnai-G2 F20). The X-ray diffraction (XRD) analysis was conducted by Bruker AXS D8 advance diffractometer with Cu-Ka source. The functional groups were detected by Fourier transform infrared spectrum (FTIR, NICOLET, 5700) in KBr pellet at 25 °C. The surface elemental compositions were detected through X-ray photoelectron spectroscopy (XPS, Thermo Fisher Scientific, UK) [1]. The UV-vis diffuse-reflectance spectra (UV-vis DRS) was performed with a Varian Cary 300 spectrometer equipped with an integrating sphere. Photoluminescence (PL) spectroscopy was performed on PerkinElmer LS-55 spectrofluorimeter at the excitation wavelength of 450 nm [24]. The photoelectrochemical experiments were carried on a CHI 660C electrochemical analyzer (CHI 660C, China) in a three-electrode cell, and the related information was shown in supplementary information (SI). The electron spin resonance (ESR) signals

were examined on a Bruker ER200-SRC spectrometer under visible light illumination ($\lambda$ > 420nm). The total organic carbon (TOC) data were obtained by a Shimadzu TOC-VCPH analyzer [1].

### 2.4. Electronic structure calculations

The electronic structure calculations of band structure and density of states were performed using Cambridge Serial Total Energy Package (CASTEP) method of Materials Studio (MS) program based on density functional theory (DFT). The generalized gradient approximation-Perdew Burke Ernzerhof (GGA-PBE) was employed as the exchange-correlation function [35-37]. SFC tolerance and energy cutoff were $1 \times 10^{-6}$ eV/atom and 220 eV for $Bi_2S_3$, and $2 \times 10^{-6}$ eV/atom and 300 eV for $Ag_3PO_4$, $Bi_2O_3$ and $Ag_3PO_4/Bi_2S_3/Bi_2O_3$. Monkhorst-Pack point k-point sets of 1 × 1 × 1, 2 × 7 × 2, 1 × 2 × 1 and 2 × 3 × 1 for $Ag_3PO_4$, $Bi_2S_3$, $Bi_2O_3$ and $Ag_3PO_4/Bi_2S_3/Bi_2O_3$, respectively. The outer valence electron arrangement of each element was $2s^2\ 2p^4$ for O, $3s^2\ 3p^3$ for P, $3s^2\ 3p^4$ for S, $4d^{10}\ 5s^1$ for Ag, $6s^2\ 6p^3$ for Bi [37, 38].

### 2.5. Photocatalytic evaluation

The photocatalytic performance of the prepared photocatalysts was assessed by degrading 10 mg $L^{-1}$ SAZ and CLX antibiotics. Detailly, 100 mg of photocatalysts was added to 100 mL of antibiotic solution. Before illumination, the mixture was stirred in dark for 30 min to achieve adsorption-desorption equilibrium. Afterward, photocatalytic tests were performed under the visible light illumination (the 300W

Xenon lamp (PLS-SXE300, Perfectlight corporation, Beijing) was served as the photo source, $\lambda > 420$ nm, the average visible light intensity was ca. 100 mW $cm^{-2}$ measured by a light meter (HS1010)). At a given time interval, 1 mL mixture was sucked out and then filtrated (0.45 μm) for detection. For investigating the dominating radical species in the photocatalytic process, the scavenger tests also were performed. Three typical reagents, i.e. TEA, BQ, and IPA were introduced as the scavengers of $h^+$, superoxide radical ($\cdot O_2^-$) and hydroxyl radical (·OH), respectively. In details, 1 mmol of TEA, BQ, or IPA was added to the photocatalytic system in the photodegradation of antibiotics by ABB-3 composite. After the photocatalytic experiments, the concentrations of SAZ and CLX were detected by an HPLC Series 1100 (Agilent, Germany) equipped with a UV-vis detector. The column was C-18 column (4.6 × 250 mm) at room temperature, and the injection volume was 20 μL. The mobile phase was water-acetonitrile (80:20, v/v) with 0.1% acetic acid for SAZ, and the phosphate buffer-acetonitrile-methanol (64:27:9 v/v) for CLX, at the flow rate was 1.0 mL $min^{-1}$. The wavelength of the detector was 270 nm and 225 nm for SAZ and CLX, respectively.

## 3. Results and discussion

### 3.1. Characterization of samples

#### 3.1.1 Morphology, crystal and chemical states analysis

The morphology of as-prepared samples was investigated by FESEM and TEM

technologies (Fig. 2). As displayed in Fig. 2A and E, the $Bi_2O_3$ was amorphous block, sharp edges and smooth surface, and the $Ag_3PO_4$ was an asymmetric particle (Fig. 2B and F) [1, 8]. For the $Bi_2S_3/Bi_2O_3$ composite, as displayed in Fig. 2C and G, the $Bi_2S_3$ was nanowire structure, and disorderly grown on the surface of $Bi_2O_3$ [11]. As for the $Ag_3PO_4/Bi_2S_3/Bi_2O_3$ composite (Fig. 2D and H), when the $Ag_3PO_4$ was introduced, it is obvious that the small particles of $Ag_3PO_4$ grown along the $Bi_2S_3$ nanowire. However, the large particles of $Ag_3PO_4$ were randomly attached on the surface of the $Bi_2S_3/Bi_2O_3$ composite. Furthermore, the detailed crystal structure of the obtained samples was performed by HRTEM technology. As showed in Fig. 2I, the lattice fringe of 0.329 nm was ascribed to the (120) plane of the $Bi_2O_3$ [24]. The lattice fringe of 0.360 nm was ascribed to the (130) plane of the $Bi_2S_3$ [25]. For the $Ag_3PO_4/Bi_2S_3/Bi_2O_3$ composite, as shown in Fig. 2J, it is clear that the coexistence of $Ag_3PO_4$, $Bi_2S_3$, and $Bi_2O_3$ phases, and the lattice fringes of 0.266 nm correlate with the (210) plane of the $Ag_3PO_4$. In addition, the more details of $Ag_3PO_4/Bi_2S_3/Bi_2O_3$ composite were performed by elemental mapping and the EDS analysis. The elemental mapping images (Fig. 2K) indicated that the uniform distribution of Ag, Bi, S, P and O elements within $Ag_3PO_4/Bi_2S_3/Bi_2O_3$ composite. Meanwhile, the EDS analysis confirmed that the $Ag_3PO_4/Bi_2S_3/Bi_2O_3$ composite was contained of Ag, Bi, S, P and O elements (Fig. 3A), and the approximate content of each element in $Ag_3PO_4/Bi_2S_3/Bi_2O_3$ composite was showed. These above results affirmed that the coexistence of $Ag_3PO_4$, $Bi_2S_3$, and $Bi_2O_3$ in nanocomposite.

The XRD patterns were performed to explore the crystal texture and composition

of the obtained samples. As showed in Fig. 3B, it could be found that all of the characteristic peaks of pure $Ag_3PO_4$ correspond to the crystalline cubic phase of $Ag_3PO_4$ (JCPDS No. 06-0505) [19], and the sharp diffraction peaks of $Ag_3PO_4$ indicated the good crystallinity. For the pure $Bi_2O_3$, all characteristic peaks perfectly indexed to the standard monoclinic phase α-$Bi_2O_3$ (JCPDS No. 41-1449) [39], and the pattern of $Bi_2S_3$ could be easily indexed to the pure orthorhombic phase structure (JCPDS No.17-0320) [40]. As for the composite samples, it could be observed that the most characteristic peaks were attributed to $Bi_2O_3$, which could be caused by the high content of $Bi_2O_3$ in the composites. Meanwhile, the characteristic peaks of $Ag_3PO_4$ or $Bi_2S_3$ could also be found. Especially for $Ag_3PO_4/Bi_2S_3/Bi_2O_3$ composites, it was obvious that they all displayed the similar characteristic peaks. However, differently, the characteristic peaks intensity of $Ag_3PO_4$ increased gradually with the increase of the content of $Ag_3PO_4$.

The typical functional groups of the as-prepared samples were studied by FTIR spectra. As displayed in Fig. 3C, for the pure $Ag_3PO_4$, the broad absorptions at around 2400-3600 $cm^{-1}$ and 1660 $cm^{-1}$ represent intrinsic OH stretching and bending vibrations [41]. The absorption at about 1400 $cm^{-1}$ is ascribed to the OH vibrations of $H_2O$ molecules adsorbed on the sample surface [41]. The bands at about 550 $cm^{-1}$ and 1010 $cm^{-1}$ correspond to the P-O stretching vibration in $PO_4^{3-}$ [17]. For the pure $Bi_2O_3$, the bands located at 3460 $cm^{-1}$ and 1640 $cm^{-1}$ could be ascribed to OH stretching and bending vibrations [21]. The absorption at about 1380 $cm^{-1}$ is assigned to the OH vibrations of $H_2O$ molecules adsorbed on the sample surface [41]. The absorption

band at 510 $cm^{-1}$ and 650 $cm^{-1}$ is attributed to the Bi-O stretching pattern [21, 29]. For the pure $Bi_2S_3$, the absorption band at 510 $cm^{-1}$ and 640 $cm^{-1}$ is ascribed to the Bi-S stretching mode [21]. As for the composites, it is obvious that the characteristic vibrations for all single-phase are coexistence in the composite. Furthermore, the specific surface area and pore properties of $Ag_3PO_4$, $Bi_2O_3$, $Bi_2S_3/Bi_2O_3$, and the ABB-3 composite were studied by $N_2$ adsorption-desorption analysis. As displayed in Fig. 3D and Table 1, although a mesoporous structure (type-IV isotherm with an H3 hysteresis loop) existed in four samples, they all exhibited relatively low specific surface area and pore volume, which could adverse to the adsorption of antibiotics by them.

The surface chemical states of AP and ABB-3 samples were investigated by XPS, and the details were displayed in Fig. 4. According to the XPS survey spectra (Fig. 1A), the AP sample contained Ag, C, O, and P elements. However, the ABB-3 sample contained Ag, C, O, P, S, and Bi elements, indicating the successful fabrication of hybrid composite. Moreover, the high-resolution XPS spectra of Ag 3d, P 2p, O 1s, Bi 4f, and S 2p were exposed. Basing on the Fig. 4B, obviously, the Ag 3d spectra of AP and ABB-3 included four characteristic peaks, the strong peaks at 373.7 and 367.8 eV indexed to Ag $3d_{3/2}$ and Ag $3d_{5/2}$ are characteristics of $Ag^+$, and the weak peaks at 374.2 and 367.2 eV can owe to the Ag $3d_{3/2}$ and Ag $3d_{5/2}$ signals of metallic Ag [16, 42]. Compared to the AP, the Ag 3d spectra of ABB-3 composite could also be divided into four characteristic peaks. Differently, the states of Ag shifted slightly towards higher binding energy, implying that others component in ABB-3 composite

could affect Ag oxidization state. Fig. 4C displayed the P 2p spectrum, the peak located at 132.6 eV, affirming that the valence state of P is +5 value [16]. As for the O 1s spectrum (Fig. 4D), the peaks presented at 530.4 eV and 531.8 eV of AP could owe to the $O^{2-}$ in the $Ag_3PO_4$ and the surface-absorbed hydroxyl oxygen [16, 18]. However, the O 1s spectrum of ABB-3 composite could be divided into three characteristic peaks, and the new peak located 533.4 eV could be attributed to the $O^{2-}$ in the $Bi_2O_3$ [1]. The Bi 4f and S 2p spectrum of BO and ABB-3 composite were showed in Fig. 4E. It was clear that the Bi 4f of BO included two characteristic peaks, and the peak at 163.9 eV and 158.6 eV should be attributed to Bi $4f_{5/2}$ and Bi $4f_{7/2}$ in $Bi_2O_3$, respectively [42]. However, the Bi 4f of ABB-3 included four characteristic peaks. In detail, the peaks at 164.3 eV and 158.8 eV could be assigned to Bi $4f_{5/2}$ and Bi $4f_{7/2}$ in $Bi_2O_3$, respectively; and the peaks at 163.4 eV and 158.0 eV corresponds to Bi $4f_{5/2}$ and Bi $4f_{7/2}$ in $Bi_2S_3$, respectively. Meanwhile, the peak centered at 162.1 eV should be ascribed to S 2p transition [21, 43], and the peak centered at 225.9 eV (Fig. 4F) should be ascribed to $S^{2-}$ [11]. Furthermore, as we can see, the peak intensity of pure material (AP and BO) is higher than those of ABB-3 composite, which should due to the lower content in ABB-3 compared to those in the pure material. Therefore, the XPS results further indicated the co-existence of $Ag_3PO_4$, $Bi_2S_3$, and $Bi_2O_3$ in the ABB-3 composite.

### 3.1.2 Optical characteristics analysis

The optical characteristics of the obtained samples were studied by UV-vis DRS,

photoelectrochemical test and PL technologies. As depicted in Fig. 5A, the optical absorption edge of pure $Bi_2O_3$ and $Ag_3PO_4$ were about 450 nm and 530 nm, respectively. The results were consistent with previous studies [24, 44]. For the pure $Bi_2S_3$, it could be found the $Bi_2S_3$ could dramatically absorb all photons in the range of UV and visible light [26]. As for the composites, it is clearly seen that the significantly enhanced visible light absorption, which could owe to the photosensitization of $Bi_2S_3$ and the formation of heterojunction [21, 26, 45]. Furthermore, the $E_g$ of the pure semiconductor was estimated from the Tauc's equation: $\alpha h\nu = A(h\nu - E_g)^{n/2}$ [26], where α, h, ν and A represent the absorption coefficient, Planck constant, light frequency and a constant, respectively. The value of n depends on the semiconductor type, n=1 and 4 for direct ($Bi_2O_3$) and indirect ($Ag_3PO_4$, $Bi_2S_3$) band-gap semiconductor, respectively. According to the calculation, the $E_g$ of $Ag_3PO_4$, $Bi_2S_3$, and $Bi_2O_3$ were 2.36, 1.29, and 2.76, respectively (Fig. 5B), which were corresponded with previous studies [1, 23, 46].

To investigate the photocurrent responses and photogenerated charges recombination probability of the AP, BO, BS, and ABB-3, the transient photocurrent test was investigated [1, 9]. As displayed in Fig. 5C, the highest current intensity of ABB-3 composite was approximately 148.20 nA $(cm^2)^{-1}$ under visible light illumination, and it was approximately 1.39, 2.01 and 3.89 times than that of AP, BO, and BS, respectively. Obviously, the ABB-3 composite possesses the superior photocurrent response, manifesting the higher separation efficiency of photogenerated $e^-$-$h^+$ pairs and faster electron transfer at the interface [1]. Simultaneously, the charge

migration rate was evaluated according to the arc radius in the electrochemical impedance spectra (EIS). It is generally believed that the smaller arc in the EIS signifies the less charge transfer resistance [1, 9]. As showed in Fig. 5D, it is obvious that the ABB-3 composite possesses the lowest charge migration resistance because of the smallest arc in the EIS. The efficient transient photocurrent response and in apparent charge migration resistance of ABB-3 composite could be attributed to the formation of the heterojunction between $Ag_3PO_4$, $Bi_2S_3$, and $Bi_2O_3$. The high photocurrent response and rapid photoexcited $e^-$-$h^+$ pairs separation of ABB-3 composite, which would endow it the excellent photocatalytic performance.

The photoluminescence (PL) spectra a very effective technique to study the transfer and recombination process of photogenerated carriers. As displayed in Fig. 5E, all samples performed significant emissions around 523-532 nm due to the recombination of $e^-$-$h^+$ pairs. However, the ABB-3 composite exhibited the lower PL emission intensity than other samples, indicating the ABB-3 composite possesses slower recombination of the $e^-$-$h^+$ pairs and the superior photocatalytic performance. The synergistic effect between $Ag_3PO_4$, $Bi_2S_3$ and $Bi_2O_3$, and the forming of heterojunction make for promoting the charge separation efficiency, decreasing the recombination of $e^-$-$h^+$ pairs effectively and lengthening charge carriers lifetime [1, 47, 48].

### 3.1.3 Band structure and density of states analysis

The electronic structure of $Ag_3PO_4$, $Bi_2S_3$, $Bi_2O_3$ and $Ag_3PO_4/Bi_2S_3/Bi_2O_3$

samples were be calculated in the MS program. The building initial unit cells confirmed by XRD and HRTEM, the optimized geometric structures of $Ag_3PO_4$ (space group No. 218; P4-3N), $Bi_2S_3$ (space group No. 62; PNMA), $Bi_2O_3$ (space group No. 114; P4-21C) and $Ag_3PO_4/Bi_2S_3/Bi_2O_3$ composite were shown in Fig. 6, the $Ag_3PO_4/Bi_2S_3/Bi_2O_3$ composite consists of a surface layer and a 15 Å of vacumm slab. Meanwhile, the lattice parameters of the samples were listed in Table 2, the lattice types of $Ag_3PO_4$, $Bi_2S_3$, $Bi_2O_3$ and $Ag_3PO_4/Bi_2S_3/Bi_2O_3$ was cubic, orthorhombic, tetragonal and triclinic, respectively. Further, band structures and the density of states (DOS) (including the total DOS (TDOS) and the projected DOS (PDOS)) of the samples were displayed in Fig. 7 and Fig. 8. It is well known that the energy levels and the $E_g$ play a significant role in determining the photocatalytic performance of the photocatalyst [35]. According to the calculation, the $E_g$ of $Bi_2S_3$ was 1.324, it is very close to experimental value. The $E_g$ of $Ag_3PO_4$ and $Bi_2O_3$ was 0.346 and 1.806, respectively, it is consistent with the previous studies [36, 37]. However, it is obvious that these calculated values are much smaller than those of the experimental values, which could be attributed to the inherent defect of DFT methods [38, 49]. Meanwhile, The $E_g$ of $Ag_3PO_4/Bi_2S_3/Bi_2O_3$ composite almost could not be figured out by this means (only 0.059 eV). Besides, the semiconductor type of $Ag_3PO_4$, $Bi_2S_3$ and $Bi_2O_3$ could be determined through the corresponding band structure. As showed in Fig. 7A, the valence band top (VBT) and conduction band bottom (CBB) of $Ag_3PO_4$ was located at M point and G point, respectively, it indicated that the $Ag_3PO_4$ is an indirect band-gap semiconductor. Ma et al. [49] also reported that the $Ag_3PO_4$ is an indirect

band-gap semiconductor according to theoretical calculation. However, the VBT of $Bi_2S_3$ was located at Y point, and the CBB of $Bi_2S_3$ closed to S point (Fig. 7B). For the $Bi_2O_3$ (Fig. 7C), the VBT and CBB both located at G point. These results indicated that the $Bi_2S_3$ and $Bi_2O_3$ is indirect and direct band-gap semiconductor, respectively they are consistent with Zahedi′s [35] and Yin et al.′s [36] studies. At the same time, it is consistent with the experimental results [49, 50]. Besides, as displayed in Fig. 7, the band structure diagram was corresponded to the DOS diagram. When the curve was more intensive in the band structure diagram, the higher peak value in the corresponding DOS diagram, which indicates the more electrons there are, otherwise, the fewer electrons there are. The more electrons should contribute to producing more carriers in the photocatalytic process [35, 38]. Obviously, the band structure of $Ag_3PO_4/Bi_2S_3/Bi_2O_3$ composite is more intensive than that of three single-phase semiconductor, which could due to the forming of the heterojunction, thus it could perform better photocatalytic performance. In details, the TDOS and PDOS revealed orbital states of electrons in the samples [37, 38]. As displayed in Fig. 8A, the VBT of $Ag_3PO_4$ comprised hybridized Ag 4d and O 2p orbitals, whereas the CBB was mainly derived from hybridized Ag 5s, Ag 5p and P 3p orbitals. Ma et al. [37] also reported the similar results. For the $Bi_2S_3$ and $Bi_2O_3$ (Fig. 8B and C), the VBT and CBB both were mainly formed by Bi 6p and S 3p orbitals. The results are similar to previous studies [35, 41, 51]. As for the $Ag_3PO_4/Bi_2S_3/Bi_2O_3$ composite (Fig. 8D), the VBT was occupied by Ag 4d, Bi 6p, O 2p and S 3p orbitals, whereas the CBB was majorly composed of Bi 6p and S 3p orbitals. Consequently, the VBT of the

$Ag_3PO_4/Bi_2S_3/Bi_2O_3$ composite has been upshifted, which should owe to the hybridization of the Ag 4d, Bi 6p, O 2p and S 3P orbitals, and the $E_g$ of the composite will be narrow. The narrowed $E_g$ is conducive to the transfer of photogenerated electrons, increasing light absorption region, thus improving the photocatalytic performance of the photocatalyst [37, 38].

### 3.2. Photocatalytic performance

The photocatalytic performance of the obtained photocatalysts was assessed towards the decomposition of two common antibiotics (namely SAZ and CLX) under visible light illumination. Meanwhile, the effects of initial antibiotic concentrations, reaction pH, supporting electrolytes and surfactants on photocatalytic performance had been investigated. Furthermore, the photostability and mineralization capacity of the as-prepared samples were also evaluated for the practical application.

#### 3.2.1 Photodegradation of SAZ and CLX

The photocatalytic efficiency of SAZ and CLX by as-prepared photocatalysts had been displayed in Fig. 9A and B. Before illumination, the mixture was stirred in dark for 30 min to achieve adsorption-desorption equilibrium, and all obtained samples possess insignificant adsorption quantity for both two antibiotics. The poor adsorption activity of these photocatalysts should be on account of the low specific surface area according to the $N_2$ adsorption-desorption results. Meanwhile, the negatively charged photocatalyst surface (Table 3) would be not conducive to the adsorption of negatively charged antibiotic molecules (pKa=7.59 for SAZ and

pKa=2.78 for CLX, data from https://pubchem.ncbi.nlm.nih.gov/) [9, 52]. Nonetheless, under the visible light illumination for 90 min, the removal efficiency of two antibiotics was increased significantly for all photocatalysts. As depicted in Fig. 9A, the ABB-3 composite exhibited the higher photocatalytic efficiency for SAZ degradation in comparison to the single-phase photocatalysts (BS, BO, AP) and other composites (ABB-1, ABB-2, ABB-4), and they were in the order of ABB-3 > ABB-2 > ABB-4 > ABB-1 > AP > BO > BS. In detail, the photocatalytic efficiency of SAZ was 98.06%, 95.78%, 94.73%, 93.01%, 87.35%, 32.17% and 15.67% for ABB-3, ABB-2, ABB-4, ABB-1, AP, BO and BS, respectively. For CLX (Fig. 9B), the removal behavior was similar to that of the SAZ, i.e., and the photocatalytic efficiency was followed ABB-3 > ABB-2 > ABB-4 > ABB-1 > AP > BO > BS. However, the photocatalysts performed a little bit lower photocatalytic activity of CLX, and the highest degradation efficiency was 90.26%. Obviously, although the increasing of $Ag_3PO_4$ content has a positive influence on the antibiotics degradation, if the content of $Ag_3PO_4$ was too high (ABB-4), the photocatalytic performance of photocatalyst would reduce, which should due to the separation efficiency of photogenerated carriers of ABB-3 and ABB-2 was superior than that of ABB-4, and the photocorrosion will be more likely to occur [53]. Furthermore, the different degradation efficiency of SAZ and CLX in the photodegradation process could due to their distinguishing structures, as showed in Fig. S1, the CXL possesses the more complex chemical structure than SAZ, meanwhile, the pKa value of SAZ is higher than that of CLX, which would be not conducive to the photodegradation of CLX [1,

3]. Compared to the single-phase photocatalysts, the increased photocatalytic efficiency of antibiotics for composites should be attributed to the forming of heterojunction among BS, BO and AP. The synergistic action between each component could increase visible light absorption, accelerate electrons transfer and the separation of $e^-$-$h^+$ (confirmed by UV-vis DRS, photocurrent test and PL spectra), which was consistent with the previous similar reports [23, 25, 26]. For deepening the comprehension of the photocatalytic behavior, the experimental results were further assessed by pseudo-first-order (PFO) kinetic model, and the results were shown in SI.

### 3.2.2 Effect of supporting electrolytes

As is known to all, the chlorine, sulfate and bicarbonate ions are the most frequent anions in the aquatic environment, which could disturb the photocatalytic process in the practical application [9, 54]. In this study, NaCl, $Na_2SO_4$, and $Na_2CO_3$ were introduced to study the detail influence on the photodegradation of two antibiotics by ABB-3 composite. As displayed in Fig. 10A and B, the photocatalytic efficiency of SAZ and CLX both decreased in different degrees in the presence of 0.05 M above electrolytes, and the decreasing in order of $Na_2CO_3$ > NaCl > $Na_2SO_4$. Basing on previous studies, bicarbonate and carbonate ions could act as the radical scavengers [9, 55], thus the photocatalytic efficiencies of SAZ and CLX decreased obviously from 98.06% and 90.26% to 78.18% and 70.59%, respectively, within the $Na_2CO_3$ electrolyte. For NaCl and $Na_2SO_4$ electrolyte, the competitive adsorption between $Cl^-$ (or $SO_4^{2-}$) and antibiotic should be responsible for the decreasing of

photocatalytic efficiency [9], that could be supported by a decreasing of absorption in dark (Fig. 10A and B). Furthermore, the competing adsorption between antibiotic molecules and $Na^+$ on the active sites of ABB-3 composite could also cause the lower photocatalytic efficiency. Additionally, the chloride and sulfate anions are also radical scavengers, which could justify their negative effect on the antibiotics degradation [9].

### 3.2.3 Effects of initial antibiotic concentrations

In practical wastewater, the initial concentration of a pollutant is fluctuating in various time. Therefore, it is significant to study the photocatalytic performance of photocatalyst under the different initial concentrations of pollutant [56, 57]. The Fig. 10C and D showed two antibiotics degradation in different initial concentrations using ABB-3 composite. It is obvious that the initial concentration exerted an important influence on the whole photocatalytic process. The photocatalytic efficiency of SAZ was 99.52%, 98.06%, 93.03%, 76.35% and 63.59% at the initial concentration was 5, 10, 20, 30 and 40 mg/L, respectively. For CLX, the photocatalytic efficiency was 98.12%, 90.26%, 84.00%, 73.35% and 55.02% at the initial concentration were 5, 10, 20, 30 and 40 mg/L, respectively. Although the photocatalytic efficiency decreases with increasing initial concentration, the actual removal of antibiotics from 4.976 mg $L^{-1}$ increased to 25.436 mg $L^{-1}$ for SAZ, and 4.906 mg $L^{-1}$ increased to 22.008 mg $L^{-1}$ for CLX. Obviously, high initial concentration could cause a negative effect in the photocatalytic rate (Fig. S3), which due to the high initial concentration of pollutant

could reduce light penetration and photon energy [9]. Meanwhile, the intermediate products increase as the initial concentrations increase, thus more competitive adsorption will occur between SAZ or CLX antibiotic molecules and intermediate products, and these results are very similar to previous studies [58]. The high initial concentration (20, 30 and 40 mg $L^{-1}$) would suppress the photocatalytic rate of ABB-3 composite in some degree, however, high antibiotic removal at low concentrations (5 mg $L^{-1}$) was considered to be of a great importance, therefore, the initial antibiotic concentration was selected as 10 mg $L^{-1}$ in the whole experiments.

### 3.2.4 Effects of reaction pH

The reaction pH is another important factor in the photocatalytic system, which could influence the generation of ROSs [2]. In this study, a series of pH values (3.00, 5.00, 6.85, 9.00, 11.00) were adjusted by NaOH (0.1 M) or $HNO_3$ (0.1 M) to investigate the influence of initial pH in the photocatalytic reaction. As displayed in Fig. 10E and F, when the initial pH was close to neutral (pH=6.85), the ABB-3 composite possesses the highest photocatalytic performance for both SAZ and CLX degradation under visible light illumination. However, the photodegradation efficiency inhibited obviously with the increase or decrease of pH value. Especially at the pH values were 3.00 and 11.00, the photodegradation efficiency only was 65.06% and 57.44% for SAZ, and 60.72% and 51.33% for CLX, respectively. The reason might be that the ABB-3 composite was partly dissolved in the strongly acidic condition, resulting in a loss quality of catalyst. Meanwhile, at the high pH condition,

although the adsorption efficiency increased [9], the excessive antibiotic adsorption could interfere light reaching the photocatalyst surface, decrease the surface light intensity, and hinder the $e^-$-$h^+$ photogeneration process. Beside, at the high pH, the negatively charged photocatalyst surface impeded the adsorption of hydroxide ion, leading to the reduction of hydroxyl radical generation. Furthermore, because at basic pH both SAZ and CLX are negatively charged, thus, repulsion between antibiotics and material is present. Consequently, absorption and degradation are disfavored. Therefore, the pH value of the degradation system has an important influence on the photocatalytic performance the synthesized composites, and the optimum reaction pH value should be set close to neutral.

### 3.2.5 Effects of surfactants

The surfactant is a widespread pollutant in wastewater, which could affect the photocatalytic performance of photocatalyst in the practical application [59-61]. In this study, two common surfactants, namely anionic SDBS and cationic CTAB, had been adopted to study the influence of surfactants on the photocatalytic process of antibiotics by ABB-3 composite catalysis. As displayed in Fig. 11A and B, the SDBS showed different effects for the SAZ and CLX degradation. When the surfactant concentration was 0.1 CMC, SDBS could promote the photodegradation of SAZ. However, the inhibiting effect happened when the surfactant concentrations were 0.3, 0.6 and 1.0 CMC. For CLX, the inhibiting effect happened at all concentration gradients. Especially in the concentration was 1.0 CMC, the inhibiting effect

happened significantly for both SAZ and CLX. When adding the CTAB (Fig. 11C and D), the low concentration of CTAB could increase the photocatalytic efficiency of both SAZ and CLX, but the inhibiting effect happened at high concentration. Furthermore, both anionic SDBS and cationic CTAB could increase the adsorption of antibiotics by ABB-3 composite. These above results are similar to those of previous studies [62-64], and the different effects happened could be summarized as the following reasons: (1) When the concentration of surfactants was low, the antibiotic molecules could interact with surfactants, while surfactants can interact with material surfaces, thus rendering the antibiotic more available to the catalytic center, which could facilitate the adsorption of antibiotics and accelerate the photodegradation of antibiotics [62-64]. [63]; (2) At the high concentration of surfactants, although the adsorption of antibiotics increased, the surfactants tend to form micelles, which could package the antibiotic molecule thus hindering the photodegradation of antibiotics. Meanwhile, the high concentration of surfactants could reduce light penetration to the surface of the photocatalyst, thus restraining the photocatalytic performance. Furthermore, the competitive adsorption and degradation could easily happen between antibiotics and surfactants at the high concentration surfactants [63-67].

### 3.2.6 Photostability and mineralization capacity tests

The mineralization efficiency and photostability (namely the chemical state (including composition and structure) and the photocatalytic performance of the photocatalyst will not be changed under the illumination) are two very important

indicators for the practical application of the photocatalyst. As displayed in Fig. 13A, the ABB-3 composite exhibited the high mineralization efficiency for both SAZ and CLX, it was 85.00% and 75.10%, respectively, under the illumination of 3 h. To study the photostability of $Ag_3PO_4$ and the ABB-3 composite, the SAZ and CLX photocatalytic tests of $Ag_3PO_4$ and the ABB-3 composite were carried out for four cycles under visible light illumination. After each cycle, the photocatalyst was recovered by centrifugation, rinsing and drying for the next cycle. As displayed in Fig. 12A and C, the photodegradation efficiencies of SAZ and CLX by the ABB-3 composite were declined in 17.18% and 15.67%, respectively, after four cyclic tests. However, the photodegradation efficiencies of SAZ and CLX by the $Ag_3PO_4$ were declined in 31.07% and 25.95%, respectively, after four cyclic tests. In the meantime, the crystal texture of $Ag_3PO_4$ and the ABB-3 composite had also been studied, as displayed in Fig. 12B and D, a new diffraction peak appeared at 38.1° in their XRD patterns, which should correspond to the (1 1 1) plane of metallic silver due to the happen of photocorrosion [68]. Grilla et al. [53] found the same phenomenon in the photocatalytic of sulfamethoxazole by $Ag_3PO_4/WO_3$ composites. Otherwise, their XRD patterns had no significant change after the cyclic tests. Thus, the decrease of photocatalytic performance could be caused by the occurrence of some photocorrosion. Meanwhile, several cycle experiments will reduce the available active sites of the photocatalyst to some extent due to the adsorbed antibiotic molecules or intermediate products that had not been completely mineralized or washed away, thus reducing the photocatalytic performance of photocatalyst. These results indicated that

although some photocorrosion would happen in ABB-3 composite, it still exhibited favorable photostability and mineralization capacity, and could performe great application potential in practical.

### 3.3. Photocatalytic mechanism

The ABB-3 composite exhibited excellent photocatalytic performance for antibiotic degradation, which could owe to the generation of some radical species in the photocatalytic process [69]. As displayed in Fig. 13B, while 1 mmol of IPA was added into the photodegradation system, the photodegradation efficiency of two antibiotics was decreased slightly, which indicated that few ·OH participated in the antibiotic degradation. Differently, when 1 mmol of TEA or BQ was added into the photodegradation process, the photodegradation of two antibiotics was restrained significantly. The degradation efficiency of SAZ and CLX decreased to 29.83%, 36.45% and 24.19%, 35.49% in the presence of TEA, BQ, respectively. The results indicated that the $h^+$ and $\cdot O_2^-$ both played important roles in the photodegradation of two antibiotics. To further verify the point, a $N_2$ purging test was also performed. The results indicated that the photodegradation efficiency of two antibiotics was depressed obviously, which confirmed the dissolved oxygen plays an important role in the generation of $\cdot O_2^-$ radical species [9]. Consequently, it could be preliminarily concluded that $h^+$ and $\cdot O_2^-$ produced in the photocatalytic process could be responsible for the improved photocatalytic performance towards antibiotics degradation.

To validate the existence of these radical species in the photocatalytic system under visible illumination, the ESR test with DMPO technique was employed. All the tests were performed under the dark condition and visible light illumination of 4 min and 8 min. As showed in Fig. 13C and D, it is obvious that there is no peak formed under the dark condition for both DMPO-·$O_2^-$ and DMPO-·OH. Whereas, under the visible light illumination, the characteristic peaks of both DMPO-·$O_2^-$ and DMPO-·OH were obvious, and the signal intensity increased with the increase of illumination time. The results verified that the ·$O_2^-$ and ·OH generated in the ABB-3 photocatalytic system. The scavenger experiments and ESR results both proved that the $h^+$, ·$O_2^-$, and ·OH worked together in the photocatalytic of two antibiotics by ABB-3 composite.

Basing on the above experimental results, a plausible photocatalytic mechanism of antibiotics by ABB-3 composite was presented. Beforehand, the VB and CB positions of three semiconductors can be determined by the following equation: $E_{VB}$=X-$E^e$+1/2$E_g$, $E_{CB}$=$E_{VB}$-$E_g$, where the X is the absolute electronegativity of the semiconductor, and the value of X is approximately 6.24 eV, 5.56 eV and 5.96 eV for $Bi_2O_3$, $Bi_2S_3$ and $Ag_3PO_4$, respectively [19]. $E^e$ is the energy of free electrons on the hydrogen scale (approximately 4.5 eV). Therefore, the $E_{VB}$ is 3.08 eV, 1.71 eV and 2.64 eV for $Bi_2O_3$, $Bi_2S_3$ and $Ag_3PO_4$, respectively, and the $E_{CB}$ is 0.41 eV, 0.42 eV and 0.28 eV, respectively.

As is well-known, the potential of VB and CB could determine the oxidbillity and reducibility of the photocatalyst, respectively [70]. When combined with $Bi_2O_3$,

$Bi_2S_3$ and $Ag_3PO_4$, the heterojunction photocatalyst will be constructed, and two likely charge separation approaches of photogenerated $e^-$-$h^+$ may be present between $Bi_2O_3$, $Bi_2S_3$ and $Ag_3PO_4$ (i.e. p-n heterojunction photocatalytic mechanism and double Z-scheme photocatalytic mechanism). As showed in Fig. 14, firstly, before contact, the Fermi levels of p-type $Bi_2O_3$ ($E_{Fp}$) was close to VB, whereas $Bi_2S_3$ and $Ag_3PO_4$ are n-type semiconductors with the Fermi level ($E_{Fn}$) close to their CB [1, 71]. However, when they contacted with each other to form a heterojunction, the energy levels of the $Bi_2O_3$ shift upward, whereas those of $Bi_2S_3$ and $Ag_3PO_4$ shift downward until the Fermi levels of $Bi_2O_3$, $Bi_2S_3$ and $Ag_3PO_4$ reached an equilibrium ($E_F$). Consequently, the CB bottom of $Bi_2O_3$ moved up to the negative potential and higher than those of $Bi_2S_3$ and $Ag_3PO_4$, while the VB top of $Bi_2S_3$ and $Ag_3PO_4$ became more positive than that of $Bi_2O_3$ [22, 72]. When the ABB-3 composite presented to visible light, the photogenerated $e^-$ will migrate from VB into CB and remaining holes in the VB for three semiconductors. If followed the p-n heterojunction photocatalytic mechanism, the $e^-$ on the CB of the $Bi_2O_3$ would transfer to the CB of $Bi_2S_3$ and $Ag_3PO_4$, and the $h^+$ transferred in the opposite direction. The $e^-$ will accumulate to the CB of $Bi_2S_3$ and $Ag_3PO_4$, and the $h^+$ will accumulate to the VB of $Bi_2O_3$ [22, 71]. If reasonable, the accumulated $e^-$ on the CB of $Bi_2S_3$ and $Ag_3PO_4$ could not reduce $O_2$ to produce $\cdot O_2^-$ because the CB of $Bi_2S_3$ and $Ag_3PO_4$ was more positive than the potential of $O_2/\cdot O_2^-$ (-0.33 eV) [70]. Additionally, the holes on the VB of $Bi_2O_3$ could not oxidize $OH^-$ or $H_2O$ to generate $\cdot OH$ due to the VB potential of $Bi_2O_3$ was lower than the standard redox potential of $OH^-/\cdot OH$ (2.40 eV) and $H_2O/\cdot OH$ (2.72 eV) (Fig.

14) [24]. Nevertheless, the above experimental results indicated that the $h^+$, $\cdot O_2^-$, and ·OH were the major active species in the ABB-3 photocatalytic system, indicating the separation approach of the photogenerated $e^-$-$h^+$ pairs could not obey the p-n heterojunction photocatalytic mechanism. The second approach was the double Z-scheme photocatalytic mechanism (Fig. 14), i.e., the $e^-$ on the CB of $Bi_2S_3$ and $Ag_3PO_4$ could transfer to the VB of $Bi_2O_3$, and then transfer to the CB of $Bi_2O_3$. After that, the accumulated $e^-$ in $Bi_2O_3$ CB possesses more negative potential for reducing $O_2$ to form $\cdot O_2^-$, and the $h^+$ retained in $Bi_2S_3$ and $Ag_3PO_4$ VB possesses more positive potential to oxidize $OH^-$ and $H_2O$ to produce ·OH [73]. Hence, it verified that the ABB-3 heterojunction follows the double Z-scheme photocatalytic mechanism. Furthermore, the UV-vis DRS results indicated that the $Bi_2S_3$ could serve as a photosensitization, which will increase the response and absorption of visible light by the heterojunction, thus further improving the photocatalytic performance of heterojunction. Therefore, the remarkable photocatalytic performance of ABB-3 composite could be ascribed to the combined action of the double Z-scheme photocatalytic system and the photosensitization of $Bi_2S_3$.

## 4. Conclusions

Herein, the novel visible light photocatalyst $Ag_3PO_4/Bi_2S_3/Bi_2O_3$ were prepared by the facile method. The composite, which contains 20% of $Ag_3PO_4$ (namely ABB-3) exhibited the higher photocatalytic performance of antibiotics (namely SAZ and CLX) than the single-phase photocatalysts and other composites under the visible light

illumination. Furthermore, the effects of initial antibiotic concentrations, reaction pH, supporting electrolytes and surfactants on photocatalytic performance had also been investigated. The results indicated that the superior photocatalytic performance would be performed under low initial antibiotic concentrations, neutral pH, no supporting electrolytes and low surfactant concentrations conditions. Variety characterization techniques further manifested that the promoted photocatalytic performance of ABB-3 composite owed to the photosensitization of $Bi_2S_3$ and the double Z-scheme photocatalytic mechanism, which significantly improved visible light absorption and hindered the $e^-$-$h^+$ pairs recombination. Meanwhile, the theoretical calculations based on DFT also indicated that the $Ag_3PO_4/Bi_2S_3/Bi_2O_3$ composite could show high photocatalytic performance due to the narrow band gap. The scavenger experiments and ESR results verified that active substances $h^+$, $\cdot O_2^-$, and ·OH worked together in the photocatalytic system. Besides, the cyclic tests indicated that the ABB-3 composite showed favorable photostability after four times recycle, which is important for the practical application of photocatalyst. This study provides a new idea for the construction of novel and efficient heterogeneous photocatalysts, which benefits the practical application in environmental remediation.

## Acknowledgments

The study was financially supported by the Program for Changjiang Scholars and Innovative Research Team in University (IRT-13R17), the National Natural Science Foundation of China (51679085, 51521006, 51508177), the Fundamental Research

Funds for the Central Universities of China (No. 531107050930), the Funds of Hunan Science and Technology Innovation Project (No. 2018RS3115). The special support for the application of computing science from High-performance Computing Center of Guangxi University.

## References

[1] B. Shao, Z. Liu, G. Zeng, Z. Wu, Y. Liu, M. Cheng, M. Chen, Y. Liu, W. Zhang, H. Feng, Nitrogen-doped hollow mesoporous carbon spheres modified g-C3N4/Bi2O3 direct dual semiconductor photocatalytic system with enhanced antibiotics degradation under visible light, ACS Sustainable Chemistry & Engineering (2018).

[2] J.J. López-Peñalver, M. Sánchez-Polo, C.V. Gómez-Pacheco, J. Rivera-Utrilla, Photodegradation of tetracyclines in aqueous solution by using UV and UV/H2O2 oxidation processes, Journal of Chemical Technology & Biotechnology 85 (2010) 1325–1333.

[3] E.S. Elmolla, M. Chaudhuri, Photocatalytic degradation of amoxicillin, ampicillin and cloxacillin antibiotics in aqueous solution using UV/TiO2 and UV/H2O2/TiO2 photocatalysis, Desalination 252 (2010) 46-52.

[4] C. Liang, C.-G. Niu, L. Zhang, X.-J. Wen, S.-F. Yang, H. Guo, G.-M. Zeng, Construction of 2D heterojunction system with enhanced photocatalytic performance: Plasmonic Bi and reduced graphene oxide co-modified Bi5O7I with high-speed charge transfer channels, Journal of hazardous materials 361 (2019) 245-258.

[5] M. Cheng, G. Zeng, D. Huang, C. Lai, Y. Liu, C. Zhang, J. Wan, L. Hu, C. Zhou, W. Xiong, Efficient degradation of sulfamethazine in simulated and real wastewater at slightly basic pH values using Co-SAM-SCS /H2O2 Fenton-like system, Water Research 138 (2018) 7-18.

[6] N. Shao, J. Wang, D. Wang, P. Corvini, Preparation of three-dimensional Ag3PO4/TiO2@MoS2 for enhanced visible-light photocatalytic activity and anti-photocorrosion, Applied Catalysis B: Environmental 203 (2017) 964-978.

[7] J. Chao, G. Liu, L. Zu, Q. Yao, J. Yang, Preparation of Ag@Ag3PO4@ZnO ternary heterostructures for photocatalytic studies, Journal of Colloid & Interface Science 453 (2015) 36-41.

[8] X. Liu, J. Xu, Z. Ni, R. Wang, J. You, R. Guo, Adsorption and visible-light-driven photocatalytic properties of Ag3PO4/WO3 composites: A discussion of the mechanism, Chemical Engineering Journal 356 (2019) 22-33.

[9] F. Chen, Q. Yang, X. Li, G. Zeng, D. Wang, C. Niu, J. Zhao, H. An, T. Xie, Y. Deng, Hierarchical assembly of graphene-bridged Ag3PO4/Ag/BiVO4 (040) Z-scheme photocatalyst: An efficient, sustainable and heterogeneous catalyst with enhanced visible-light photoactivity towards tetracycline degradation under visible light irradiation, Applied Catalysis B: Environmental 200 (2017) 330-342.

[10] A.B. Trench, T.R. Machado, A.F. Gouveia, M. Assis, L.G. da Trindade, C. Santos, A. Perrin, C. Perrin, M. Oliva, J. Andrés, E. Longo, Connecting structural, optical, and electronic properties and photocatalytic activity of Ag3PO4:Mo complemented by DFT calculations, Applied Catalysis B:

Environmental 238 (2018) 198-211.
[11] L. Chen, J. He, Q. Yuan, Y. Liu, C.-T. Au, S.-F. Yin, Environmentally benign synthesis of branched Bi2O3–Bi2S3 photocatalysts by an etching and re-growth method, Journal of Materials Chemistry A 3 (2015) 1096-1102.
[12] Y. Shi, Y. Chen, G. Tian, H. Fu, K. Pan, J. Zhou, H. Yan, One-pot controlled synthesis of sea-urchin shaped Bi2S3/CdS hierarchical heterostructures with excellent visible light photocatalytic activity, Dalton Transactions 43 (2014) 12396-12404.
[13] C. Zhou, P. Xu, C. Lai, C. Zhang, G. Zeng, D. Huang, M. Cheng, L. Hu, W. Xiong, X. Wen, L. Qin, J. Yuan, W. Wang, Rational design of graphic carbon nitride copolymers by molecular doping for visible-light-driven degradation of aqueous sulfamethazine and hydrogen evolution, Chemical Engineering Journal 359 (2019) 186-196.
[14] W. Jiang, W. Luo, R. Zong, W. Yao, Z. Li, Y. Zhu, Polyaniline/Carbon Nitride Nanosheets Composite Hydrogel: A Separation-Free and High-Efficient Photocatalyst with 3D Hierarchical Structure, Small 12 (2016) 4370-4378.
[15] D. Xia, Z. Shen, G. Huang, W. Wang, J.C. Yu, P.K. Wong, Red Phosphorus: An Earth-Abundant Elemental Photocatalyst for “Green” Bacterial Inactivation under Visible Light, Environmental Science & Technology 49 (2015) 6264-6273.
[16] T. Yan, J. Tian, W. Guan, Z. Qiao, W. Li, J. You, B. Huang, Ultra-low loading of Ag3PO4 on hierarchical In2S3 microspheres to improve the photocatalytic performance: The cocatalytic effect of Ag and Ag3PO4, Applied Catalysis B: Environmental 202 (2017) 84-94.
[17] L. Liu, L. Ding, Y. Liu, W. An, S. Lin, Y. Liang, W. Cui, A stable Ag3PO4@PANI core@shell hybrid: Enrichment photocatalytic degradation with π-π conjugation, Applied Catalysis B: Environmental 201 (2017) 92-104.
[18] Z. Wang, T. Hu, K. Dai, J. Zhang, C. Liang, Construction of Z-scheme Ag3PO4/Bi2WO6 composite with excellent visible-light photodegradation activity for removal of organic contaminants, Chinese Journal of Catalysis 38 (2017) 2021-2029.
[19] Z.M. Yang, G.F. Huang, W.Q. Huang, J.M. Wei, X.G. Yan, Y.Y. Liu, C. Jiao, Z. Wan, A. Pan, Novel Ag3PO4/CeO2 composite with high efficiency and stability for photocatalytic applications, Journal of Materials Chemistry A 2 (2013) 1750-1756.
[20] G. Fu, G. Xu, S. Chen, L. Lei, M. Zhang, Ag3PO4/Bi2WO6 hierarchical heterostructures with enhanced visible light photocatalytic activity for the degradation of phenol, Catalysis Communications 40 (2013) 120-124.
[21] W. Luo, F. Li, Q. Li, X. Wang, W. Yang, L. Zhou, L. Mai, Heterostructured Bi2S3-Bi2O3 Nanosheets with Built-In Electric Field for Improved Sodium Storage, Acs Applied Materials & Interfaces 10 (2018).
[22] H. Lu, Q. Hao, T. Chen, L. Zhang, D. Chen, C. Ma, W. Yao, Y. Zhu, A high-performance Bi2O3/Bi2SiO5 p-n heterojunction photocatalyst induced by phase transition of Bi2O3, Applied Catalysis B Environmental 237 (2018).
[23] Y. Huang, W. Fan, L. Bei, H. Li, F. Zhao, Z. Liu, Y. Tong, H. Ji, Visible light Bi2S3/Bi2O3/Bi2O2CO3 photocatalyst for effective degradation of organic pollutions, Applied Catalysis B Environmental 185 (2016) 68-76.
[24] L. Jiang, X. Yuan, G. Zeng, J. Liang, X. Chen, H. Yu, H. Wang, Z. Wu, J. Zhang, T. Xiong, In-situ synthesis of direct solid-state dual Z-scheme WO3/g-C3N4/Bi2O3 photocatalyst for the degradation of refractory pollutant, Applied Catalysis B: Environmental 227 (2018) 376-385.
[25] C. Yu, K. Wang, P. Yang, S. Yang, C. Lu, Y. Song, S. Dong, J. Sun, J. Sun, One-pot facile synthesis of

Bi2S3/SnS2/Bi2O3 ternary heterojunction as advanced double Z-scheme photocatalytic system for efficient dye removal under sunlight irradiation, Applied Surface Science 420 (2017).
[26] J. Ke, J. Liu, H. Sun, H. Zhang, X. Duan, P. Liang, X. Li, M.O. Tade, S. Liu, S. Wang, Facile assembly of Bi2O3/Bi2S3/MoS2 n-p Heterojunction with layered n -Bi2O3 and p -MoS2 for Enhanced Photocatalytic Water Oxidation and Pollutant Degradation, Applied Catalysis B Environmental 200 (2017) 47-55.
[27] S. Mosleh, M.R. Rahimi, M. Ghaedi, K. Dashtian, Sonophotocatalytic degradation of trypan blue and vesuvine dyes in the presence of blue light active photocatalyst of Ag3PO4/Bi2S3-HKUST-1-MOF: Central composite optimization and synergistic effect study, Ultrasonics Sonochemistry 32 (2016) 387-397.
[28] Z. Fang, Y. Liu, Y. Fan, Y. Ni, X. Wei, K. Tang, J. Shen, Y. Chen, Epitaxial Growth of CdS Nanoparticle on Bi2S3 Nanowire and Photocatalytic Application of the Heterostructure, Journal of Physical Chemistry C 115 (2011) 281-301(221).
[29] O. Mehraj, N.A. Mir, B.M. Pirzada, S. Sabir, Fabrication of novel Ag3PO4/BiOBr heterojunction with high stability and enhanced visible-light-driven photocatalytic activity, Applied Surface Science 332 (2015) 419-429.
[30] Y.L. Qi, G. Han, X.C. Song, Enhanced photocatalytic degradation of phenol over Ag3PO4-BiOCl1−xBrx composites, Materials Research Bulletin 102 (2018) 16-23.
[31] Z. Cui, M. Si, Z. Zheng, L. Mi, W. Fa, H. Jia, Preparation and characterization of Ag3PO4/BiOI composites with enhanced visible light driven photocatalytic performance, Catalysis Communications 42 (2013) 121-124.
[32] C. Li, P. Zhang, R. Lv, J. Lu, T. Wang, S. Wang, H. Wang, J. Gong, Selective Deposition of Ag3PO4 on Monoclinic BiVO4 (040) for Highly Efficient Photocatalysis, Small 9 (2013) 3950-3950.
[33] C. Zhang, K. Yu, Y. Feng, Y. Chang, T. Yang, Y. Xuan, D. Lei, L.L. Lou, S. Liu, Novel 3DOM-SrTiO3/Ag/Ag3PO4 Ternary Z-scheme Photocatalysts with Remarkably Improved Activity and Durability for Contaminant Degradation, Applied Catalysis B Environmental 210 (2017).
[34] L. Zhou, W. Zhang, L. Chen, H. Deng, J. Wan, A novel ternary visible-light-driven photocatalyst AgCl/Ag3PO4/g-C3N4: Synthesis, characterization, photocatalytic activity for antibiotic degradation and mechanism analysis, Catalysis Communications 100 (2017) 191-195.
[35] E. Zahedi, Hydrostatic pressure effects on the electronic, optical, and photocatalytic properties of ribbon-like Bi 2 S 3 : A DFT study, Superlattices & Microstructures 81 (2015) 49-63.
[36] YIN, The electron structure and photocatalytic activity of Ti(IV) doped Bi_2O_3, Science China Chemistry 54 (2011) 180-185.
[37] X. Ma, B. Lu, D. Li, R. Shi, C. Pan, Y. Zhu, Origin of Photocatalytic Activation of Silver Orthophosphate from First-Principles, Journal of Physical Chemistry C 115 (2011) 4680-4687.
[38] B. Feng, Z. Wu, J. Liu, K. Zhu, Z. Li, X. Jin, Y. Hou, Q. Xi, M. Cong, P. Liu, Combination of ultrafast dye-sensitized-assisted electron transfer process and novel Z-scheme system: AgBr nanoparticles interspersed MoO 3 nanobelts for enhancing photocatalytic performance of RhB, Applied Catalysis B Environmental 206 (2017) 242-251.
[39] R. Irmawati, M.N.N. Nasriah, Y.H. Taufiq-Yap, S.B.A. Hamid, Characterization of bismuth oxide catalysts prepared from bismuth trinitrate pentahydrate: influence of bismuth concentration, Catal. Today 93 (2004) 701-709.
[40] Y. Yan, Z. Zhou, X. Zhao, J. Zhou, A controlled anion exchange strategy to synthesize core-shell β-bismuth oxide/bismuth sulfide hollow heterostructures with enhanced visible-light photocatalytic activity, Journal of colloid and interface science 435 (2014) 91-98.

[41] S. Zhang, S. Zhang, L. Song, Super-high activity of Bi3+ doped Ag3PO4 and enhanced photocatalytic mechanism, Applied Catalysis B-Environmental 152 (2014) 129-139.
[42] F. Chen, Q. Yang, Y. Wang, J. Zhao, D. Wang, X. Li, Z. Guo, H. Wang, Y. Deng, C. Niu, Novel ternary heterojunction photcocatalyst of Ag nanoparticles and g-C3N4 nanosheets co-modified BiVO4 for wider spectrum visible-light photocatalytic degradation of refractory pollutant, Appl. Catal. B: Environ. 205 (2016) 133-147.
[43] Y. Zhang, Y. Guo, B. Fang, Y. Chen, H. Duan, H. Li, H. Liu, Continuously enhanced photoactivity of hierarchical β-Bi2O3/Bi2S3 heterostructure derived from novel BiO2CH3 octagonal nanoplates, Applied Catalysis A General 514 (2016) 146-153.
[44] Q. Xiang, L. Di, T. Shen, L. Fan, Graphene-modified nanosized Ag3PO4 photocatalysts for enhanced visible-light photocatalytic activity and stability, Applied Catalysis B Environmental 162 (2015) 196-203.
[45] M. Wang, Q. Wang, P. Guo, Z. Jiao, In situ fabrication of nanoporous BiVO4/Bi2S3 nanosheets for enhanced photoelectrochemical water splitting, Journal of colloid and interface science 534 (2019) 338-342.
[46] H. Zhang, H. Huang, H. Ming, H. Li, L. Zhang, Y. Liu, Z. Kang, Carbon quantum dots/Ag3PO4 complex photocatalysts with enhanced photocatalytic activity and stability under visible light, Journal of Materials Chemistry 22 (2012) 10501-10506.
[47] H.N. Yun, S. Ikeda, M. Matsumura, R. Amal, A perspective on fabricating carbon-based nanomaterials by photocatalysis and their applications, Energ. Environ. Sci. 5 (2012) 9307-9318.
[48] W.K. Jo, N.C.S. Selvam, Z-scheme CdS/g-C3N4 composites with RGO as an electron mediator for efficient photocatalytic H 2 production and pollutant degradation, Chem. Eng. J. 317 (2017) 913-924.
[49] Z. Ma, Z. Yi, J. Sun, K. Wu, Electronic and Photocatalytic Properties of Ag3PC4VI (C = O, S, Se): A Systemic Hybrid DFT Study, The Journal of Physical Chemistry C 116 (2012) 25074-25080.
[50] Z. Li, S. Sun, X. Xu, B. Zheng, A. Meng, Photocatalytic activity and DFT calculations on electronic structure of N-doped ZnO/Ag nanocomposites, Catalysis Communications 12 (2011) 890-894.
[51] S. Singh, R. Sharma, Bi 2 O 3 /Ni-Bi 2 O 3 system obtained via Ni-doping for enhanced PEC and photocatalytic activity supported by DFT and experimental study, Solar Energy Materials & Solar Cells 186 (2018) 208-216.
[52] F. Chen, Q. Yang, Y. Zhong, H. An, J. Zhao, T. Xie, Q. Xu, X. Li, D. Wang, G. Zeng, Photo-reduction of bromate in drinking water by metallic Ag and reduced graphene oxide (RGO) jointly modified BiVO4 under visible light irradiation, Water Research 101 (2016) 555-563.
[53] E. Grilla, A. Petala, Z. Frontistis, I.K. Konstantinou, D.I. Kondarides, D. Mantzavinos, Solar photocatalytic abatement of sulfamethoxazole over Ag3PO4/WO3 composites, Applied Catalysis B: Environmental 231 (2018) 73-81.
[54] J. Wang, L. Tang, G. Zeng, Y. Deng, Y. Liu, L. Wang, Y. Zhou, Z. Guo, J. Wang, C. Zhang, Atomic scale g-C3N4/Bi2WO6 2D/2D heterojunction with enhanced photocatalytic degradation of ibuprofen under visible light irradiation, Applied Catalysis B: Environmental 209 (2017) 285-294.
[55] H. Xiao, R. Liu, X. Zhao, J. Qu, Enhanced degradation of 2,4-dinitrotoluene by ozonation in the presence of manganese(II) and oxalic acid, Journal of Molecular Catalysis A Chemical 286 (2008) 149-155.
[56] B. Shao, Z. Liu, G. Zeng, Y. Liu, X. Yang, C. Zhou, M. Chen, Y. Liu, Y. Jiang, M. Yan, Immobilization of laccase on hollow mesoporous carbon nanospheres: noteworthy immobilization, excellent stability and efficacious for antibiotic contaminants removal, J. Hazard. Mater. (2018).

[57] S. Wu, H. Li, X. Li, H. He, C. Yang, Performances and mechanisms of efficient degradation of atrazine using peroxymonosulfate and ferrate as oxidants, Chemical Engineering Journal (2018).
[58] W. Hou, X. Yuan, W. Yan, G. Zeng, H. Dong, X. Chen, L. Leng, Z. Wu, L. Peng, In situ synthesis of In 2 S 3 @MIL-125(Ti) core–shell microparticle for the removal of tetracycline from wastewater by integrated adsorption and visible-light-driven photocatalysis, Applied Catalysis B Environmental 186 (2016) 19-29.
[59] Z. Liu, B. Shao, G. Zeng, M. Chen, Z. Li, Y. Liu, Y. Jiang, H. Zhong, Y. Liu, M. Yan, Effects of rhamnolipids on the removal of 2,4,2,4-tetrabrominated biphenyl ether (BDE-47) by Phanerochaete chrysosporium analyzed with a combined approach of experiments and molecular docking, Chemosphere 210 (2018) 922-930.
[60] B. Shao, Z. Liu, H. Zhong, G. Zeng, G. Liu, M. Yu, Y. Liu, X. Yang, Z. Li, Z. Fang, J. Zhang, C. Zhao, Effects of rhamnolipids on microorganism characteristics and applications in composting: A review, Microbiological Research 200 (2017) 33-44.
[61] W. Xue, D. Huang, G. Zeng, J. Wan, C. Zhang, R. Xu, M. Cheng, R. Deng, Nanoscale zero-valent iron coated with rhamnolipid as an effective stabilizer for immobilization of Cd and Pb in river sediments, Journal of Hazardous Materials 341 (2018) 381-389.
[62] L. Tang, J. Wang, G. Zeng, Y. Liu, Y. Deng, Y. Zhou, J. Tang, J. Wang, Z. Guo, Enhanced photocatalytic degradation of norfloxacin in aqueous Bi2WO6 dispersions containing nonionic surfactant under visible light irradiation, Journal of Hazardous Materials 306 (2016) 295-304.
[63] A.M. Khan, A. Mehmood, M. Sayed, M.F. Nazar, B. Ismail, R.A. Khan, H. Ullah, H.M.A. Rehman, A.Y. Khan, A.R. Khan, Influence of acids, bases and surfactants on the photocatalytic degradation of a model dye rhodamine B, Journal of Molecular Liquids 236 (2017) 395-403.
[64] T. Del Giacco, R. Germani, F. Saracino, M. Stradiotto, Counterion effect of cationic surfactants on the oxidative degradation of Alizarin Red-S photocatalysed by TiO2 in aqueous dispersion, Journal of Photochemistry and Photobiology A: Chemistry 332 (2017) 546-553.
[65] T. Zhang, T. Oyama, S. Horikoshi, J. Zhao, N. Serpone, H. Hidaka, Photocatalytic decomposition of the sodium dodecylbenzene sulfonate surfactant in aqueous titania suspensions exposed to highly concentrated solar radiation and effects of additives, Applied Catalysis B Environmental 42 (2003) 13-24.
[66] D. Fabbri, A.B. Prevot, E. Pramauro, Effect of surfactant microstructures on photocatalytic degradation of phenol and chlorophenols, Applied Catalysis B Environmental 62 (2006) 21-27.
[67] Y. Liu, G. Zeng, H. Zhong, Z. Wang, Z. Liu, M. Cheng, G. Liu, X. Yang, S. Liu, Effect of rhamnolipid solubilization on hexadecane bioavailability: enhancement or reduction?, Journal of Hazardous Materials 322 (2017) 394.
[68] Y. Liu, L. Fang, H. Lu, Y. Li, C. Hu, H. Yu, One-pot pyridine-assisted synthesis of visible-light-driven photocatalyst Ag/Ag3PO4, Applied Catalysis B: Environmental 115-116 (2012) 245-252.
[69] Z. Zhu, M. Murugananthan, J. Gu, Y. Zhang, Fabrication of a Z-Scheme g-C3N4/Fe-TiO2 Photocatalytic Composite with Enhanced Photocatalytic Activity under Visible Light Irradiation, Catalysts 8 (2018) 112.
[70] J. Zhang, Y. Hu, X. Jiang, S. Chen, S. Meng, X. Fu, Design of a direct Z-scheme photocatalyst: preparation and characterization of Bi2O3/g-C3N4 with high visible light activity, J. Hazard. Mater. 280 (2014) 713-722.
[71] J. Sun, X. Li, Q. Zhao, M.O. Tadé, S. Liu, Construction of p-n Heterojunction β-Bi2O3/BiVO4 Nanocomposite with Improved Photoinduced Charge Transfer Property and Enhanced Activity in

Degradation of ortho-Dichlorobenzene, Appl. Catal. B: Environ. 219 (2017) 259-268.
[72] H. Huang, Y. He, X. Du, P.K. Chu, Y. Zhang, A General and Facile Approach to Heterostructured Core/Shell $BiVO_4$/BiOI p-n Junction: Room-Temperature In Situ Assembly and Highly Boosted Visible-Light Photocatalysis, Acs Sustainable Chemistry & Engineering 3 (2017) 151021091821006.
[73] S. Chen, Y. Hu, X. Jiang, S. Meng, X. Fu, Fabrication and characterization of novel Z-scheme photocatalyst $WO_3$/g-$C_3N_4$ with high efficient visible light photocatalytic activity, Mater. Chem. Phys. 149-150 (2015) 512-521.

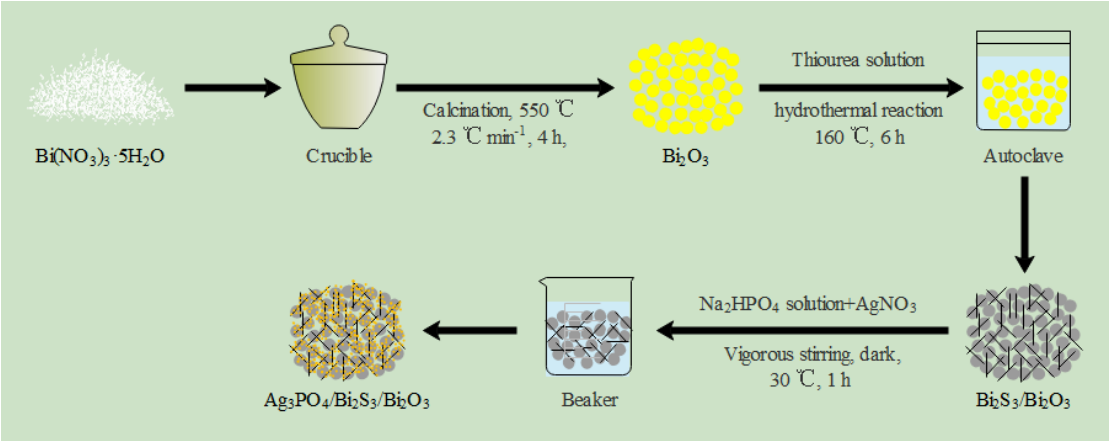
$Bi(NO_3)_3 \cdot 5H_2O$
Crucible
Calcination, 550 ℃
2.3 ℃ $min^{-1}$, 4 h,
$Bi_2O_3$
Thiourea solution
hydrothermal reaction
160 ℃, 6 h
Autoclave
$Bi_2S_3/Bi_2O_3$
$Na_2HPO_4$ solution+$AgNO_3$
Vigorous stirring, dark,
30 ℃, 1 h
Beaker
$Ag_3PO_4/Bi_2S_3/Bi_2O_3$

**Fig. 1**

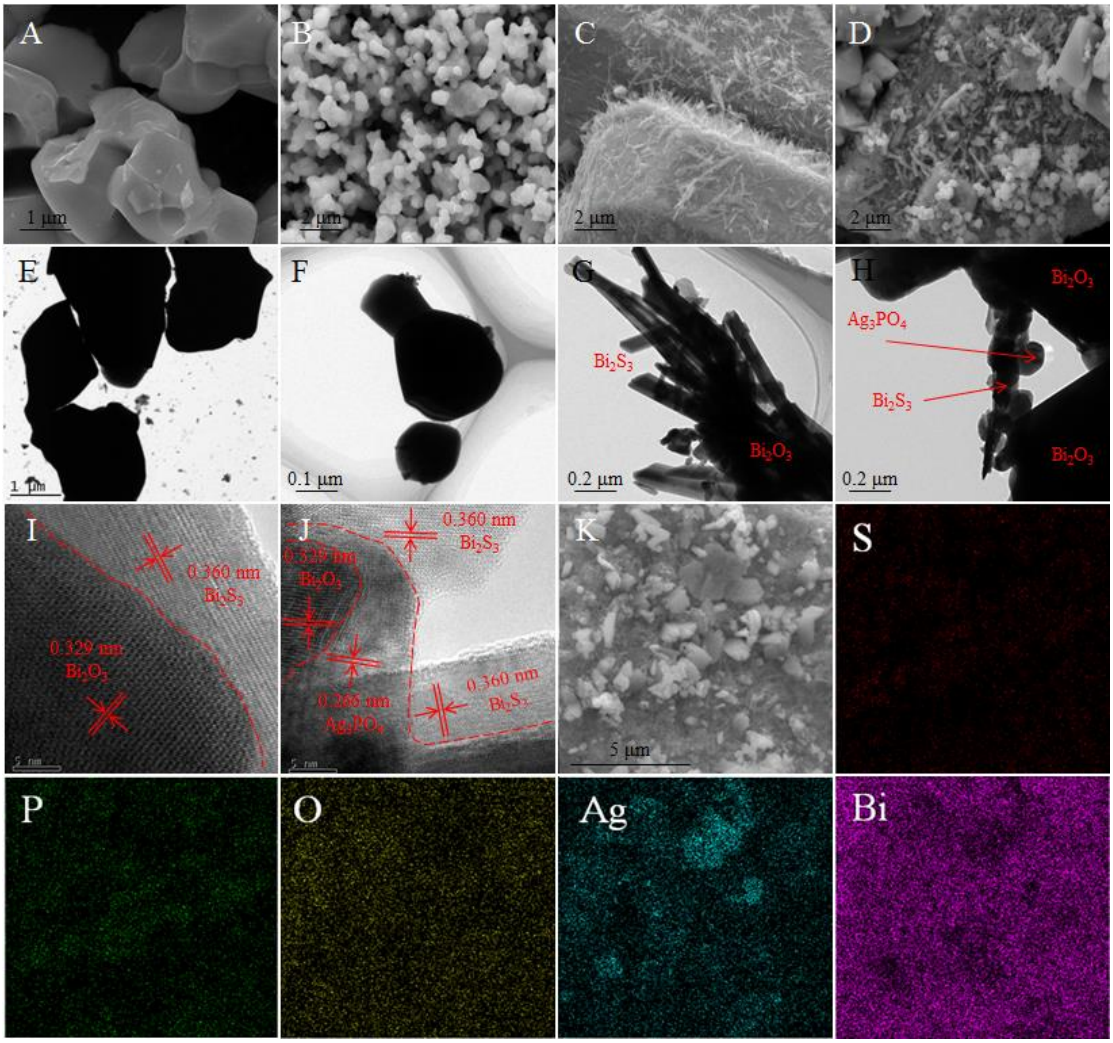
A
1 μm
B
2 μm
C
2 μm
D
2 μm
E
1 μm
F
0.1 μm
G
$Bi_2S_3$
$Bi_2O_3$
0.2 μm
H
$Bi_2O_3$
$Ag_3PO_4$
$Bi_2S_3$
$Bi_2O_3$
0.2 μm
I
0.360 nm
$Bi_2S_3$
0.329 nm
$Bi_2O_3$
J
0.360 nm
$Bi_2S_3$
0.329 nm
$Bi_2O_3$
0.268 nm
$Ag_3PO_4$
0.360 nm
$Bi_2S_3$
K
5 μm
S
P
O
Ag
Bi

**Fig. 2**

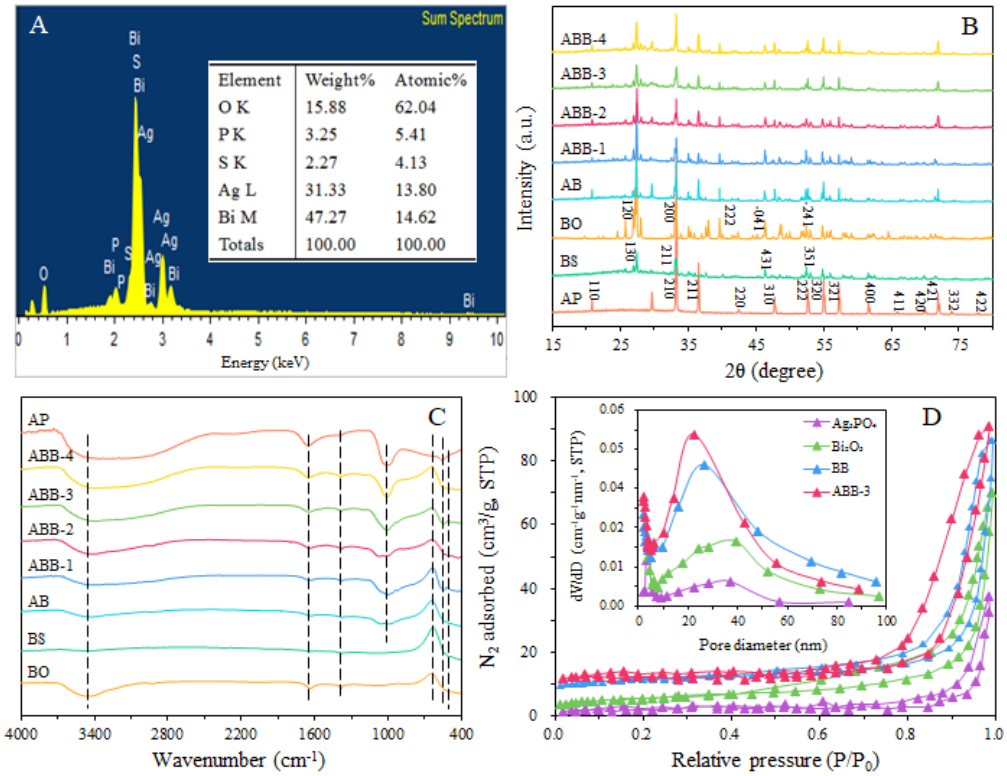
A
Sum Spectrum
Element | Weight% | Atomic%
O K | 15.88 | 62.04
P K | 3.25 | 5.41
S K | 2.27 | 4.13
Ag L | 31.33 | 13.80
Bi M | 47.27 | 14.62
Totals | 100.00 | 100.00
Energy (keV)
B
ABB-4
ABB-3
ABB-2
ABB-1
AB
BO
BS
AP
Intensity (a.u.)
2θ (degree)
C
Wavenumber (cm-1)
D
Ag3PO4
Bi2O3
BB
ABB-3
dV/dD (cm3g-1nm-1, STP)
Pore diameter (nm)
N2 adsorbed (cm3/g, STP)
Relative pressure (P/P0)

**Fig. 3**

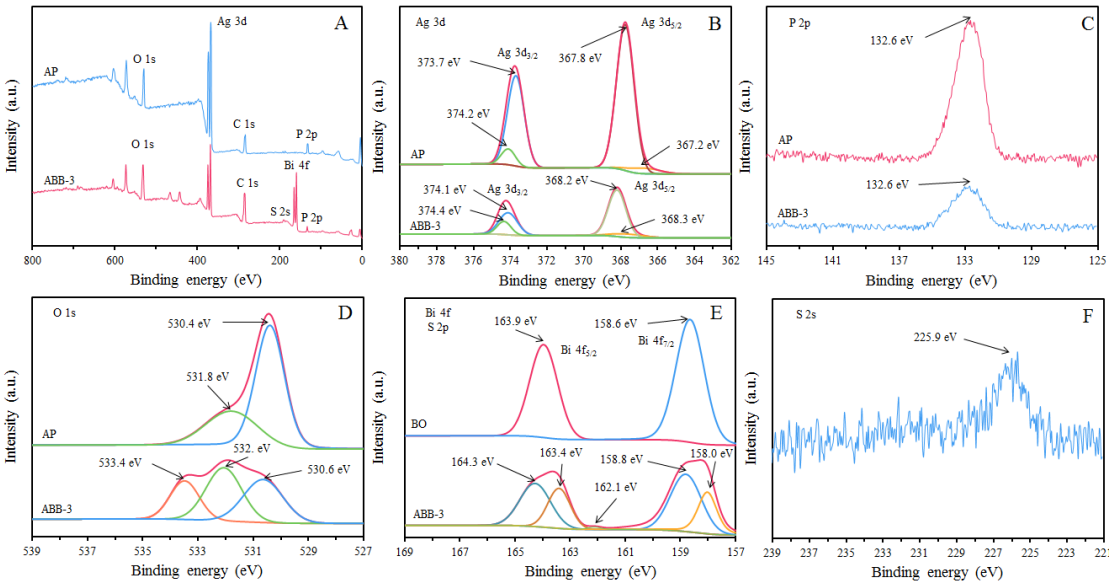
A
Ag 3d
O 1s
AP
C 1s
P 2p
O 1s
Bi 4f
ABB-3
C 1s
S 2s
P 2p
Intensity (a.u.)
Binding energy (eV)
B
Ag 3d
Ag 3d3/2
373.7 eV
374.2 eV
AP
Ag 3d5/2
367.8 eV
367.2 eV
374.1 eV
374.4 eV
ABB-3
Ag 3d3/2
368.2 eV
Ag 3d5/2
368.3 eV
C
P 2p
132.6 eV
AP
132.6 eV
ABB-3
D
O 1s
530.4 eV
531.8 eV
AP
533.4 eV
532. eV
530.6 eV
ABB-3
E
Bi 4f
S 2p
163.9 eV
Bi 4f5/2
158.6 eV
Bi 4f7/2
BO
164.3 eV
163.4 eV
158.8 eV
158.0 eV
162.1 eV
ABB-3
F
S 2s
225.9 eV

**Fig. 4**

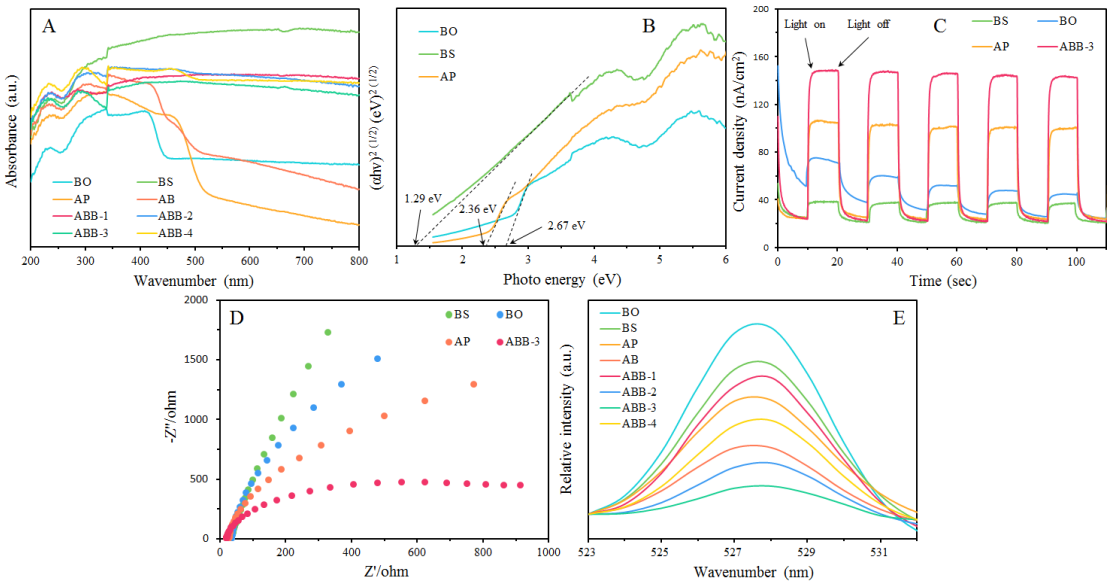
A
Absorbance (a.u.)
Wavenumber (nm)
BO
BS
AP
AB
ABB-1
ABB-2
ABB-3
ABB-4
B
(αhν)^2 (1/2) (eV)^2 (1/2)
Photo energy (eV)
1.29 eV
2.36 eV
2.67 eV
C
Light on
Light off
Current density (nA/cm^2)
Time (sec)
D
-Z''/ohm
Z'/ohm
E
Relative intensity (a.u.)
Wavenumber (nm)

**Fig. 5**

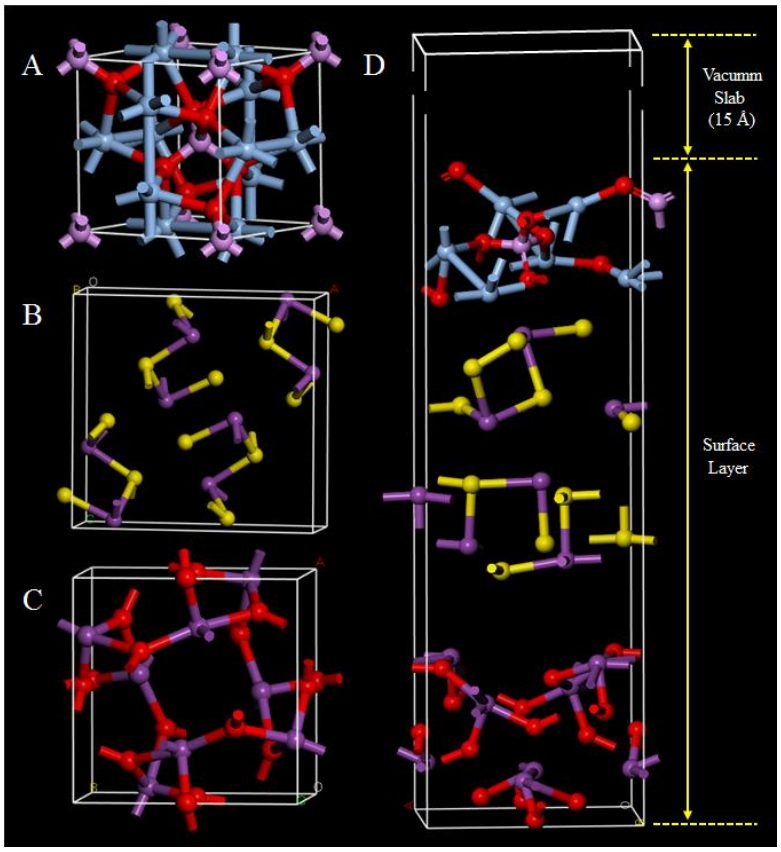


**Fig. 6**

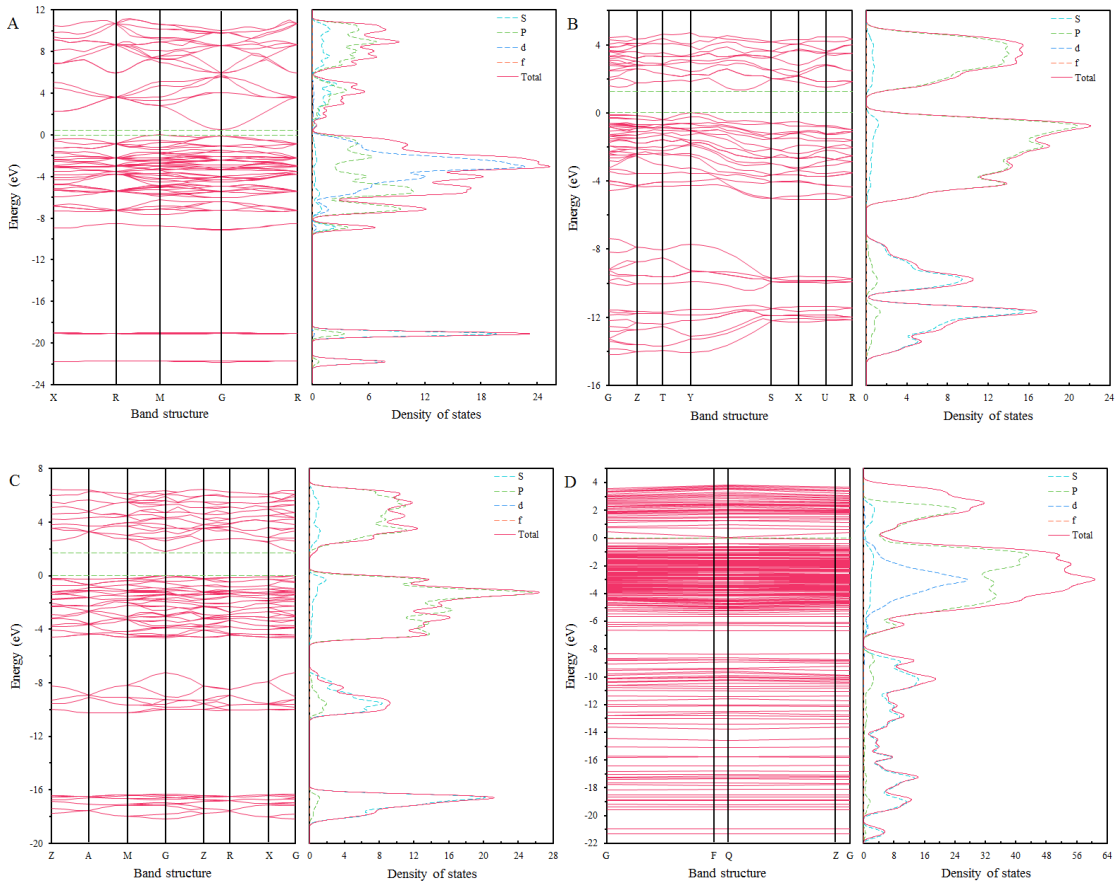
A
B
C
D
Energy (eV)
Band structure
Density of states
S
P
d
f
Total
X R M G R
G Z T Y S X U R
Z A M G Z R X G
G F Q Z G

**Fig. 7**

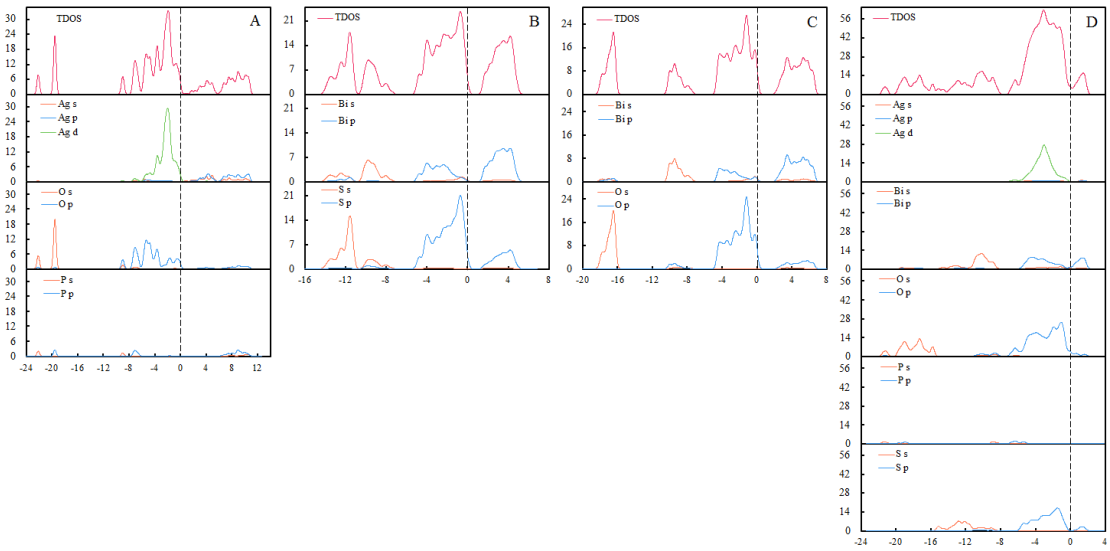
TDOS
A
Ag s
Ag p
Ag d
O s
O p
P s
P p
TDOS
B
Bi s
Bi p
S s
S p
TDOS
C
Bi s
Bi p
O s
O p
TDOS
D
Ag s
Ag p
Ag d
Bi s
Bi p
O s
O p
P s
P p
S s
S p

**Fig. 8**

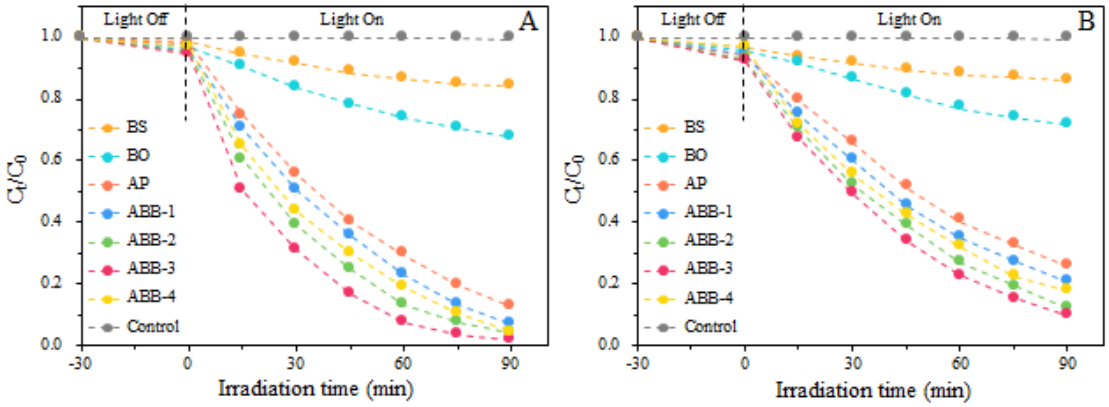
Light Off
Light On
A
B
BS
BO
AP
ABB-1
ABB-2
ABB-3
ABB-4
Control
$C_t/C_0$
Irradiation time (min)

**Fig. 9**

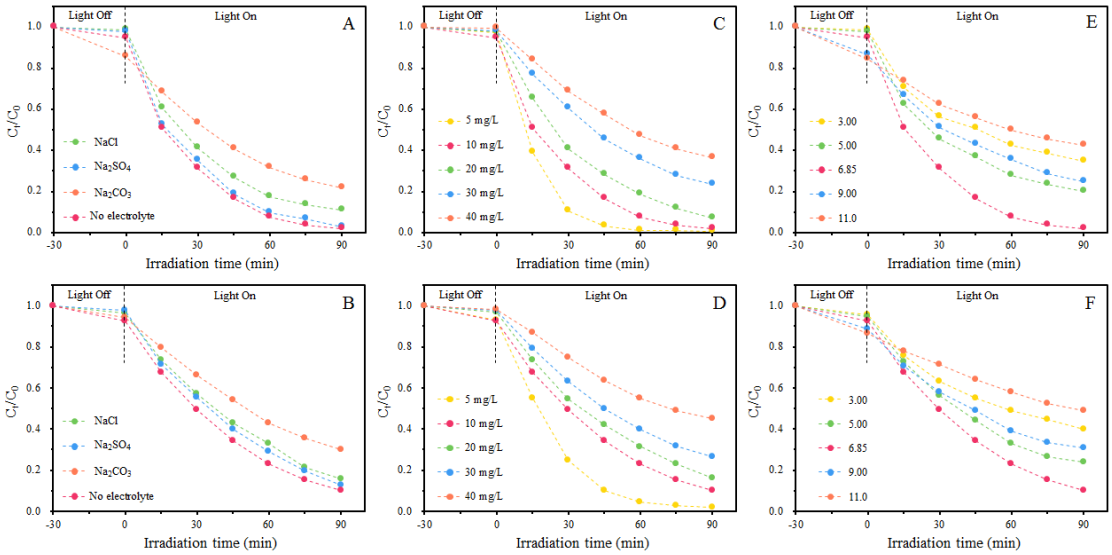
Light Off
Light On
A
B
C
D
E
F
$C_t/C_0$
Irradiation time (min)
NaCl
$Na_2SO_4$
$Na_2CO_3$
No electrolyte
5 mg/L
10 mg/L
20 mg/L
30 mg/L
40 mg/L
3.00
5.00
6.85
9.00
11.0

**Fig. 10**

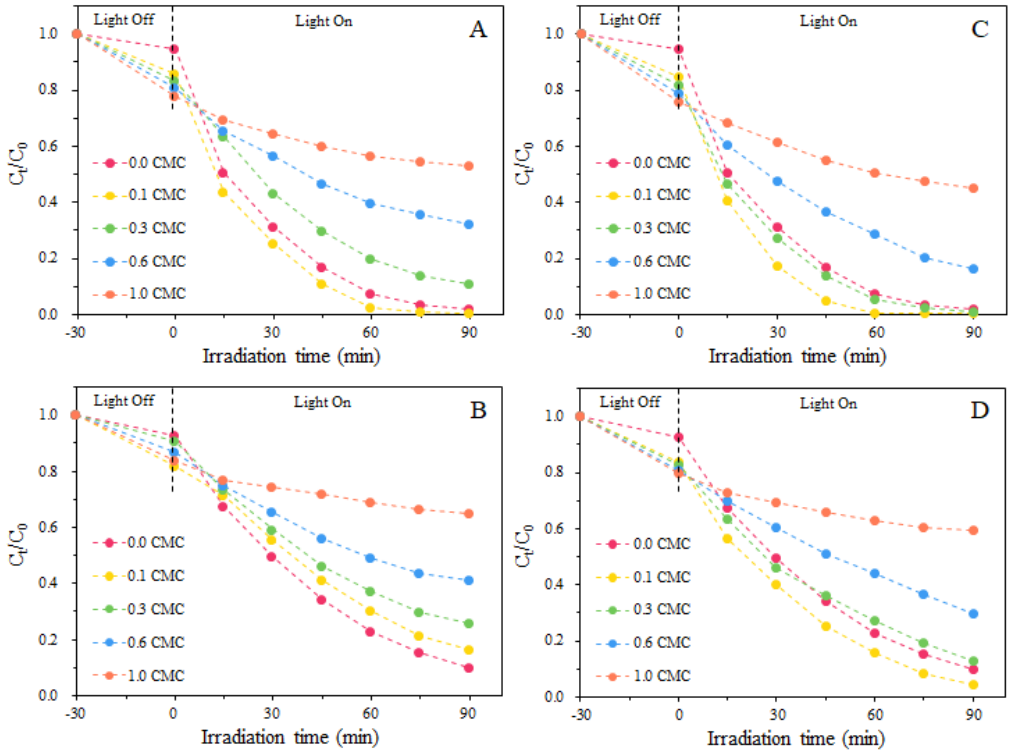
Light Off
Light On
A
B
C
D
0.0 CMC
0.1 CMC
0.3 CMC
0.6 CMC
1.0 CMC
$C_t/C_0$
Irradiation time (min)

**Fig. 11**

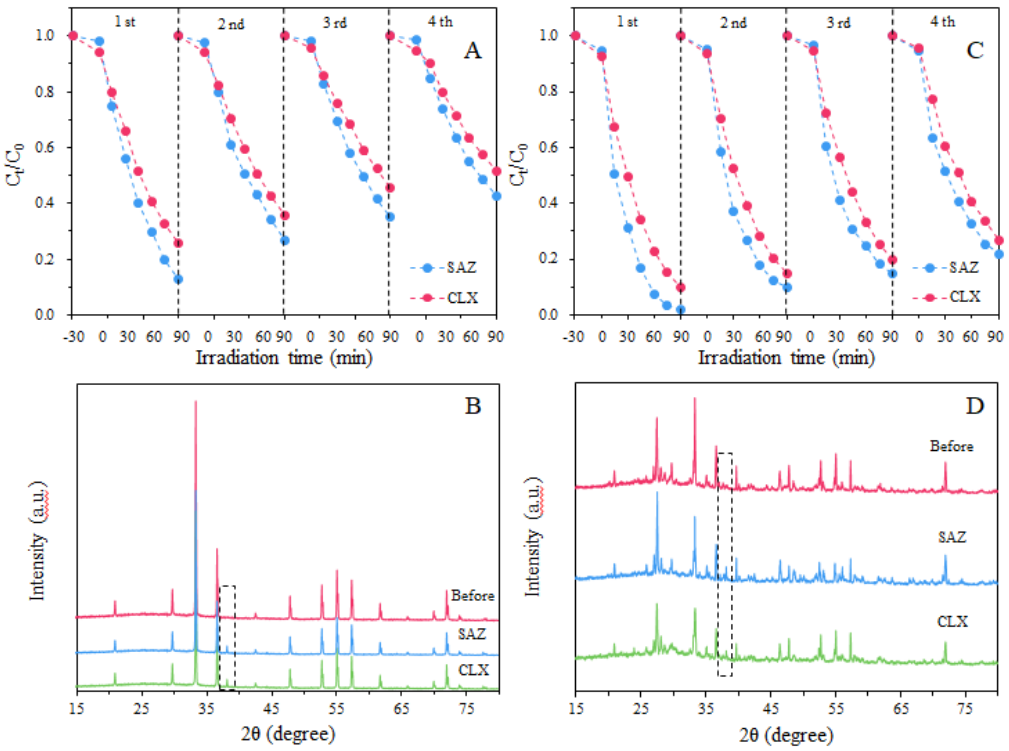
A
B
C
D
1 st
2 nd
3 rd
4 th
$C_t/C_0$
Irradiation time (min)
SAZ
CLX
Intensity (a.u.)
Before
2θ (degree)

**Fig. 12**

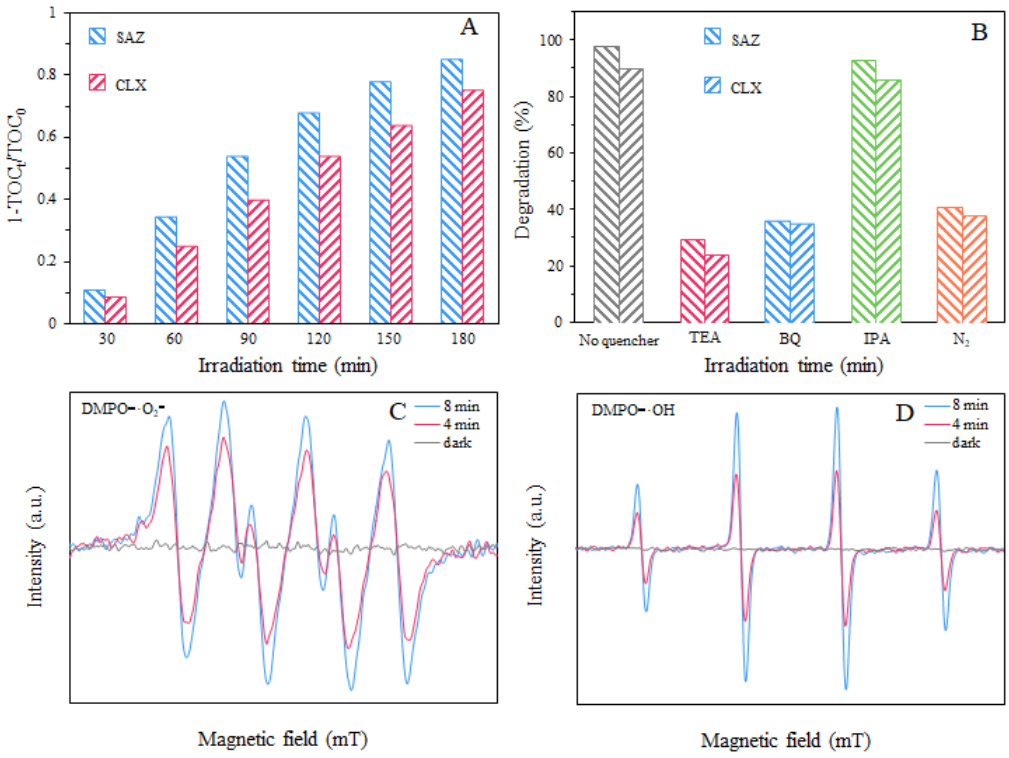
A
SAZ
CLX
1-TOC$_t$/TOC$_0$
Irradiation time (min)
B
SAZ
CLX
Degradation (%)
No quencher
TEA
BQ
IPA
$N_2$
Irradiation time (min)
C
DMPO-$\cdot O_2^-$
8 min
4 min
dark
Intensity (a.u.)
Magnetic field (mT)
D
DMPO-$\cdot$OH
8 min
4 min
dark
Intensity (a.u.)
Magnetic field (mT)

**Fig. 13**

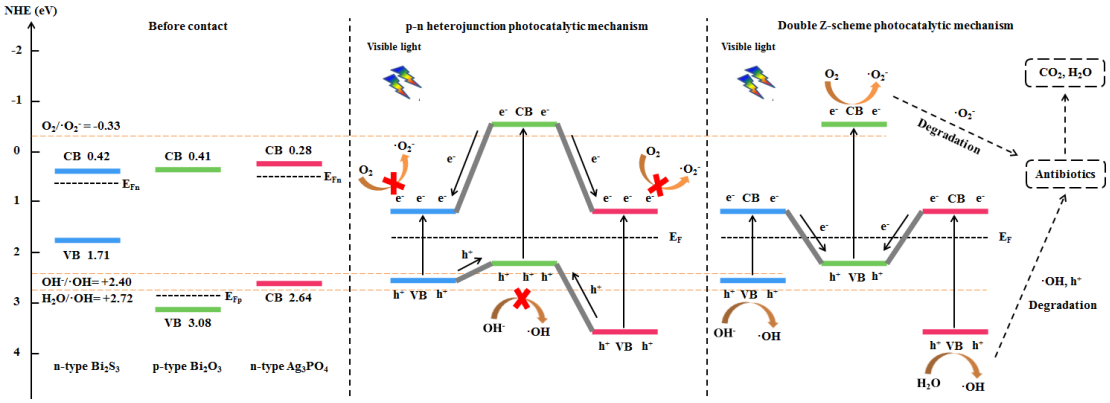
NHE (eV)
Before contact
p-n heterojunction photocatalytic mechanism
Double Z-scheme photocatalytic mechanism
Visible light
O2/·O2- = -0.33
CB 0.42
VB 1.71
CB 0.41
VB 3.08
CB 0.28
CB 2.64
OH-/·OH= +2.40
H2O/·OH= +2.72
n-type Bi2S3
p-type Bi2O3
n-type Ag3PO4
CO2, H2O
Antibiotics
Degradation
·OH, h+

**Fig. 14**

**Fig. 1** Schematic illustration of the preparation process of the $Ag_3PO_4/Bi_2S_3/Bi_2O_3$ composite.

**Fig. 2** SEM images of BO (A), AP (B), BB (C) and ABB-3 (D); TEM images of BO (E), AP (F), BB (G) and ABB-3 (H); HRTEM images of BB (I), ABB-3 (J); corresponding elemental mapping images of ABB-3 (K).

**Fig. 3** EDS patterns of ABB-3 (A); XRD patterns of the as-prepared samples (B); FTIR patterns of the as-prepared samples (C); $N_2$ adsorption-desorption analysis of the as-prepared samples (D).

**Fig. 4** XPS spectra of as-prepared samples.

**Fig. 5** UV-vis spectrum of the as-prepared samples (A); The band gap energies of AP, BS and BO (B); The transient photocurrent of the as-prepared samples (C); The EIS for different catalyst under visible light illumination (D); The photoluminescence spectra of the as-prepared samples (F).

**Fig. 6** Optimized geometric structures of $Ag_3PO_4$ (A), $Bi_2S_3$ (B), $Bi_2O_3$ (C) and $Ag_3PO_4/Bi_2S_3/Bi_2O_3$ (D). Red, blue, pink, yellow and purple spheres represent O, P, Ag, S and Bi atoms, respectively.

**Fig. 7** Band structures and the density of states of $Ag_3PO_4$ (A), $Bi_2S_3$ (B), $Bi_2O_3$ (C) and $Ag_3PO_4/Bi_2S_3/Bi_2O_3$ (D) calculated through the DFT.

**Fig. 8** TDOS and PDOS of $Ag_3PO_4$ (A), $Bi_2S_3$ (B), $Bi_2O_3$ (C) and $Ag_3PO_4/Bi_2S_3/Bi_2O_3$ (D).

**Fig. 9** The photocatalytic activities of as-prepared samples for SAZ (A) and CLX (B) degradation under visible light (Experimental conditions: initial antibiotic

concentration = 10 mg $L^{-1}$, pH = 6.85, photocatalyst dosage = 100 mg, antibiotic solution volume = 100 mL, visible light: $\lambda > 420$ nm);

**Fig. 10** Effect of supporting electrolytes for SAZ (A) and CLX (B) degradation by ABB-3 composite under visible light illumination (Experimental conditions: initial antibiotic concentration = 10 mg $L^{-1}$, pH = 6.85, ABB-3 dosage = 100 mg, antibiotic solution volume = 100 mL, visible light: $\lambda > 420$ nm); Effect of initial concentration for SAZ (C) and CLX (D) degradation by ABB-3 composite under visible light illumination (Experimental conditions: pH = 6.85, ABB-3 dosage = 100 mg, antibiotic solution volume = 100 mL, visible light: $\lambda > 420$ nm); Effect of reaction pH for SAZ (E) and CLX (F) degradation by ABB-3 composite under visible light illumination (Experimental conditions: initial antibiotic concentration = 10 mg $L^{-1}$, ABB-3 dosage = 100 mg, antibiotic solution volume = 100 mL, visible light: $\lambda > 420$ nm).

**Fig. 11** Effect of SDBS for SAZ (A) and CLX (B) degradation by ABB-3 composite under visible light illumination; Effect of CTAB for SAZ (C) and CLX (D) degradation by ABB-3 composite under visible light illumination.

**Fig. 12** The cyclic photocatalytic experiments of $Ag_3PO_4$ (A) and ABB-3 composite (B) for the degradation of antibiotics (Experimental conditions: initial antibiotic concentration = 10 mg $L^{-1}$, pH = 6.85, photocatalyst dosage = 100 mg, antibiotic solution volume = 100 mL, visible light: $\lambda > 420$ nm); The XRD pattern of $Ag_3PO_4$ (C) and ABB-3 composite (D) after 4th run cycle photocatalytic experiments.

**Fig. 13** TOC removal of SAZ and CLX by ABB-3 composite illumination for 180 min (A); Trapping experiment of radical species during the photocatalytic degradation

of two antibiotics over ABB-3 composite under visible light illumination (B); ESR spectra of radical adducts trapped by DMPO ($\bullet O_2^-$ and •OH) in ABB-3 dispersion in the dark and under visible light illumination: in methanol dispersion for DMPO-$\bullet O_2^-$ (C); in aqueous dispersion for DMPO-•OH (D).

**Fig. 14** Schematic diagram for possible charge separation and photocatalytic mechanism of ABB-3 composite.

**Table 1.** Pore structure parameters of $Ag_3PO_4$, $Bi_2O_3$, BB and ABB-3.

| Sample | BET surface area ($m^2/g$) | Pore volume ($cm^3/g$) | Average pore size (nm) |
|---|---|---|---|
| $Ag_3PO_4$ | 0.761 | 0.0059 | 5.83 |
| $Bi_2O_3$ | 1.067 | 0.0011 | 14.361 |
| BB | 5.479 | 0.0072 | 18.16 |
| ABB-3 | 6.187 | 0.0083 | 20.41 |

**Table 2.** Lattice parameters of the samples.

| Samples | Lattice types | Lengths (Å) | | | Angles (°) | | |
|---|---|---|---|---|---|---|---|
| | | a | b | c | α | β | γ |
| $Ag_3PO_4$ | 3D cubic | 5.858804 | 5.858804 | 5.858804 | 90 | 90 | 90 |
| $Bi_2S_3$ | 3D orthorhombic | 11.731377 | 3.762958 | 11.257090 | 90 | 90 | 90 |
| $Bi_2O_3$ | 3D tetragonal | 8.224678 | 8.224678 | 5.828303 | 90 | 90 | 90 |
| $Ag_3PO_4/Bi_2S_3/Bi_2O_3$ | 3D triclinic | 8.604953 | 5.948813 | 46.338558 | 90 | 90 | 90 |

**Table 3.** The Zeta potentials of ABB-3 composite in ultrapure water of different pH.

| pH | 3.00 | 5.00 | 6.85 | 9.00 | 11.00 |
|---|---|---|---|---|---|
| Zeta potential | -5.83 | -10.72 | -23.88 | -38.49 | -45.12 |

## Graphical abstract：

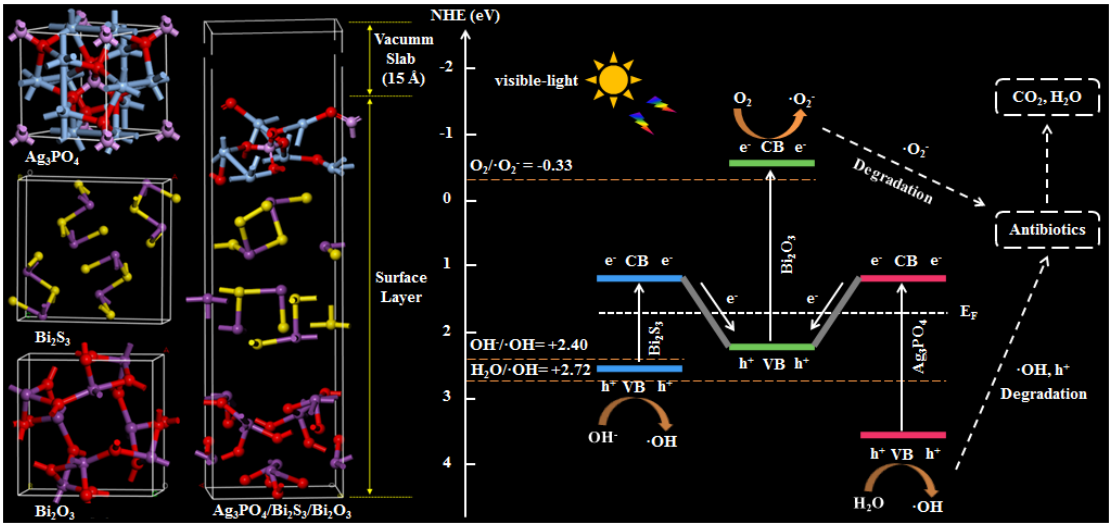

**Highlights:**

- Double Z-scheme $Ag_3PO_4/Bi_2S_3/Bi_2O_3$ photocatalyst was prepared by the facile way.
- Band structures and density of states of the samples were calculated based on density functional theory.
- The $Ag_3PO_4/Bi_2S_3/Bi_2O_3$ photocatalyst exhibited high photodegradation for antibiotics under visible light irradiation.
- $Bi_2S_3$ served as a photosensitization in the $Ag_3PO_4/Bi_2S_3/Bi_2O_3$ photocatalytic system.
- The $h^+$ and $\cdot O_2^-$ play a significant role in the photocatalytic process.